Structural Insights into Allosteric Regulation of GdpP: A Conformationally Dynamic Phosphodiesterase

Shadikejiang Shataer[1], Shannon Modla[2], Leif Boddie[1], Samiran Subedi[3], Katsuhiko Murakami[4], Mona Batish[1], and Vijay Parashar[1]*

[1]Department of Medical and Molecular Sciences, 15 Innovation Way, University of Delaware, Newark, DE, USA, 19711

[2]Delaware Biotechnology Institute, 590 Avenue 1743, Newark, DE, USA, 19713

[3]Department of Chemistry and Biochemistry, University of Delaware, Newark, DE, USA,19711

[4]Department of Biochemistry and Molecular Biology, The Center for RNA Molecular Biology, The Center for Structural Biology, Pennsylvania State University, University Park, Pennsylvania, USA

Correspondence should be addressed to: Dr. Vijay Parashar at parashar@udel.edu

Keywords

c-di-AMP, phosphodiesterase, GdpP, Cryo-EM, bacterial second messenger, PAS domain, GGDEF domain, DHH-DHHA1 domains, heme, asymmetric catalysis, allosteric regulation, structural biology

Abstract

The phosphodiesterase GdpP is a central regulator of the bacterial second messenger c-di-AMP and a key driver of antibiotic resistance in pathogenic Firmicutes. GdpP integrates environmental signals through its sensory PAS domain to control its C-terminal catalytic domain activity, but the molecular basis for this allosteric communication has remained unknown due to the lack of structural data for the complete cytosolic region. Here, we present the first Cryo-EM structures of the cytosolic region of *Streptococcus mutans* GdpP ($SmGdpP_{74}$) in multiple conformational states, revealing a sophisticated tetrameric architecture that enables asymmetric catalytic regulation. Our structural and functional analyses demonstrate that $SmGdpP_{74}$ operates through substrate-induced conformational transition, with the DHHA1 domain interface serving as the primary determinant of asymmetric catalysis. The non-canonical GGDEF domain functions as a tetrameric scaffolding hub that positions the DHH-DHHA1 catalytic domains, representing

the first detailed example of a GGDEF domain repurposed to stabilize heterologous catalytic domains. We identify a flexible GGDEF-DHH linker as a critical coupling element that transmits conformational signals between domains, with the conserved KRSR motif acting as a molecular switch for heme-mediated inhibition. Additionally, the flexibility of this linker is essential for the enzyme's catalytic activity. Based on these findings, we propose a comprehensive mechanistic model where $SmGdpP_{74}$ integrates substrate availability with conformational changes for efficient hydrolysis and allosteric control of its enzymatic activity through the PAS domain. These structural insights provide a foundation for rational drug design targeting allosteric regulatory mechanisms in GdpP, potentially offering new approaches to combat antibiotic resistance in pathogenic Firmicutes.

Introduction

Cyclic di-adenosine monophosphate (c-di-AMP) is a ubiquitous bacterial second messenger integral to cellular homeostasis, virulence, and stress adaptation. It regulates processes spanning cell wall integrity, potassium transport, DNA repair, and osmotic balance, while also modulating host immune responses through interactions with receptors like STING and NF-κB (Corrigan and Gründling, 2013; He et al., 2020). Tight control of c-di-AMP levels is critical for bacterial survival, achieved through its synthesis by diadenylate cyclases (DACs) and degradation by phosphodiesterases (PDEs) (Commichau et al., 2018). The PDEs responsible for c-di-AMP hydrolysis contain either a DHH-DHHA1 domain, as in GdpP (GGDEF domain protein containing phosphodiesterase) and DhhP, or an HD domain, as in PgpH (Huynh et al., 2015; Stülke and Krüger, 2020). GdpP (also known as YybT) is a membrane-bound, multi-domain PDE with regulatory domains that modulate its DHH-DHHA1 catalytic activity, while DhhP is a simpler, cytosolic PDE composed solely of DHH-DHHA1 domains without regulatory elements (Rao et al., 2010; He et al., 2016). Like GdpP, PgpH is membrane-bound but lacks cytosolic regulatory domains and is present in Firmicutes, though absent in *Staphylococcaceae* and *Streptococcaceae* (Huynh et al., 2015). A novel c-di-AMP-specific PDE, AtaC, identified in *Streptomyces venezuelae*, belongs to the type I PDE/nucleotide pyrophosphatase family and is found in many Actinobacteria lacking DHH-DHHA1 or HD-type PDEs (Latoscha et al., 2020). GdpP hydrolyzes c-di-AMP into the linear dinucleotide 5'-O-phosphonoadenylyl-(3'->5')-adenosine (5′-pApA) (Rao et al., 2010). Unlike standalone DHH-DHHA1 PDEs, such as *Mycobacterium tuberculosis*'s Dhhp (Rv2837c), which further degrade 5′-pApA into two AMP molecules, GdpP's activity is restricted to the first hydrolysis step (Manikandan et al., 2014; Rao et al., 2010). Although GdpP homologs can also hydrolyze c-di-GMP, c-di-AMP is generally regarded

as the physiological substrate as the Michaelis-Menten constant (K_m) for c-di-GMP is more than 300 fold higher than that for c-di-AMP (Rao et al., 2010).

GdpP comprises two N-terminal transmembrane helices anchoring it to the membrane, followed by a PAS domain, a degenerate GGDEF domain, and the C-terminal DHH-DHHA1 catalytic core (Rao et al., 2010). The PAS domain of GdpP, which features a conserved fold of antiparallel β-sheets flanked by α-helices, binds heme and allosterically inhibits the PDE activity of the DHH domains. Interestingly, when cyanide (CN^-) or nitric oxide (NO) coordinates to the heme, this inhibition is reversed, restoring the enzyme's phosphodiesterase activity (Rao et al., 2011). These findings reveal a regulatory mechanism in which heme acts as a molecular switch, modulating GdpP activity in response to environmental signals such as CN^- or NO.

The GGDEF domain, while homologous to diguanylate cyclases (DGCs) in other proteins, lacks the ability to synthesize c-di-GMP and instead exhibits weak ATPase activity, though its physiological role remains enigmatic (Rao et al., 2011, 2010). Catalytically active GGDEF domains bear GG(D/E)EF consensus motif at their active site (A-site) and a conserved RxxD motif at an inhibitory site (I-site), which binds to the product (c-di-GMP) and mediates feedback inhibition with an inhibition constant of ~1 μM (Chan et al., 2004; Sinha and Sprang, 2006). The A and I sites are located at the opposite ends of the GGDEF domain and the synthesis of c-di-GMP requires dimerization of two active GGDEF domains with the loops bearing the GGDEF motifs of each monomer brought in close proximity for the cyclization of two GTP molecules (Schirmer and Jenal, 2009). The substrate inhibition of GGDEF is believed to be achieved by a mechanism known as domain immobilization in which two intercalated c-di-GMP molecules bind to the I site of each monomer while the dimeric interface of the A sites are broken with the two A sites being too far apart from each other to be catalytically active (Deepthi et al., 2014; Vorobiev et al., 2012).

The DHH-DHHA1 domain harbors a binuclear metal center critical for catalysis, with structural flexibility between its subdomains enabling substrate accommodation. Notably, existing crystal structures of GdpP's DHH-DHHA1 domain only depict inactive conformations, with metal centers too distant for catalysis, suggesting dynamic regulation by PAS or GGDEF domains *in vivo* (Wang et al., 2018). Beyond heme-dependent inhibition, the bacterial alarmone (p)ppGpp acts as a strong competitive inhibitor of GdpP's DHH-DHHA1 phosphodiesterase domain in *B. subtilis*, *S. aureus*, and *E. faecalis* (Bowman et al., 2016; Corrigan et al., 2015; Rao et al., 2010; Wang et al., 2017). This multifactorial GdpP inhibition allows Firmicute pathogens like *S. aureus* to simultaneously elevate cellular c-di-AMP levels, thicken cell walls for β-lactam resistance and modulate host STING pathways (Griffiths and O'Neill, 2012; Poon et al., 2022). In *S. suis*, in-frame deletion of *gdpp* lead to elevated levels of cellular c-di-AMP, increased biofilm formation, and reduced virulence (Du et al., 2014). *S. pyogenes* requires functional GdpP for SpeB

protease activation and systemic infection (Cho and Kang, 2013). *Streptococcus mutans,* a primary etiological agent of dental caries, relies on GdpP-mediated c-di-AMP regulation to control biofilm formation and virulence in dental plaque. Deletion of *S. mutans gdpp* elevated cellular c-di-AMP and exacerbated biofilm formation (Lemos et al., 2019; Peng et al., 2016)

Clinically, GdpP is the most significant c-di-AMP PDE, acting as the primary regulator in major Gram-positive pathogens like *Staphylococcus aureus*, *Streptococcus pneumoniae*, and *Enterococcus faecalis* (Bai et al., 2013; Gundlach et al., 2015). Loss-of-function mutations in GdpP, common in clinical isolates, elevate c-di-AMP levels, driving increased β-lactam antibiotic tolerance and resistance independent of mechanisms like mecA (Poon et al., 2022 ; Wang et al., 2017). Unlike PgpH, which supports virulence in bacteria such as Listeria and Enterococcus but is absent in key pathogens, or AtaC, which lacks direct clinical relevance, GdpP's multi-domain structure uniquely combines environmental sensing with c-di-AMP hydrolysis. This integration makes it critical for cell wall stress adaptation and a key determinant of treatment outcomes in staphylococcal infections, highlighting its unmatched clinical importance among c-di-AMP PDEs.

Despite its central role in c-di-AMP degradation, the full-length structure of GdpP has not yet been determined. Here, we present the first structure of the cytosolic region of GdpP from *Streptococcus mutans*, capturing the enzyme in multiple conformations and revealing the reaction product within the catalytic pocket. Our results illuminate dynamic interdomain rearrangements in *S. mutans* GdpP that regulate its catalytic activity, as well as allosteric regulation by heme, providing structural blueprints for targeting dysregulated c-di-AMP degradation in Firmicutes.

Materials and Methods

Cloning, Expression, and Purification

The gene encoding the cytosolic form of GdpP from *Streptococcus mutans* strain NCTC10449 (GenBank: SQF49590.1), starting at the 74th N-terminal amino acid (termed $SmGdpP_{74}$), was amplified by PCR using primers listed in Supplementary Table 1. This PCR product was ligated into the pQLinkH plasmid backbone via In-Fusion Cloning (Takara Bio USA), yielding an N-terminally His_6-tagged $SmGdpP_{74}$-PQH wild-type plasmid (Scheich et al., 2007). Mutant variants were created by subjecting the wild-type plasmid to Q5 site-directed mutagenesis (New England Biolabs) per the manufacturer's instructions, using custom primers detailed in Supplementary Table 1.

For protein expression, the recombinant plasmids were transformed into *Escherichia coli* BL21 (DE3) cells, and transformants were selected on plates with 0.1 mg/mL ampicillin. A single colony was inoculated into 100 mL of LB medium containing 0.1 mg/mL ampicillin and incubated overnight at 37°C. From this, 50 mL was used to inoculate 2 L of LB medium with 0.1 mg/mL ampicillin. The culture was grown at 37°C with constant shaking until the optical density at 600 nm (OD_{600}) reached 0.8. Protein expression was then induced with isopropyl β-D-1-thiogalactopyranoside (IPTG) at a final concentration of 0.25 mM, and the culture was further incubated overnight at 16°C with shaking. Cells were harvested by centrifugation and resuspended in Buffer A (50 mM Tris-HCl pH 8, 200 mM NaCl, 5% glycerol, 0.05% 2-mercaptoethanol, 20 mM imidazole), supplemented with 0.1 mg/mL DNase I (Sigma-Aldrich) and 1% (v/v) protease inhibitor cocktail (Sigma-Aldrich). The cells were lysed by sonication, and the lysate was centrifuged at 50,000 g for 30 minutes. The supernatant was loaded onto a 5 mL HisTrap HP column (Cytiva Life Sciences, Inc.) pre-equilibrated with Buffer A. After washing with 10 column volumes of Buffer A, $SmGdpP_{74}$ was eluted using a gradient of Buffer B (identical to Buffer A but with 500 mM imidazole) increasing to 100% over 20 column volumes. Fractions containing $SmGdpP_{74}$ were concentrated to approximately 1 mL and purified further on a Superdex 200 size exclusion chromatography (SEC) column pre-equilibrated with Buffer C (10 mM Tris-HCl pH 8, 200 mM NaCl, 5 mM dithiothreitol). The resulting SEC fractions were collected, concentrated, aliquoted, and stored at -80°C.

For heme reconstitution, 20 μM of the SEC-purified wild-type and mutant proteins were incubated with 100 μM heme in buffer C for 2 hours before being loaded onto the Superdex 200 column. The SEC elution profile was monitored at 280 nm (to detect protein) and 420 nm (to detect heme). The heme-reconstituted protein fractions were then collected, concentrated, and stored at -80°C for future use.

Cryo-EM Data Acquisition and Image Processing

Sample Preparation

The apo $SmGdpP_{74}$ sample (0.65 mg/mL, 10 μM) was prepared directly from the SEC purification without ligands. For the heme-CN-bound sample, $SmGdpP_{74}$ (0.65 mg/mL) was incubated with 10 mM (stock concentration) heme-CN at a 1:10 molar ratio (protein:heme-CN) on ice for 30 minutes. For the pApA-bound sample, $SmGdpP_{74}$ (0.65 mg/mL) was incubated with 10 mM cyclic-di-AMP (stock concentration) at a 1:10 molar ratio for 5 minutes on ice prior to vitrification. For each condition, 2.5 μL of sample was applied to glow-discharged Ultra Au Foil R 1.2/1.3 300 mesh gold grids (Quantifoil Micro

Tools) and vitrified by plunging into liquid ethane using a Vitrobot (ThermoFisher Scientific).

Data Acquisition

Cryo-EM datasets for all three conditions (apo, heme-CN, and 5'-pApA) were collected at the Laboratory for Biomolecular Structures (LBMS) at Brookhaven National Laboratory using a Krios microscope operated at 300 keV with a K3 detector. Data collection was managed with EPU (SerialEM) software. The apo dataset was acquired at a nominal magnification of 87,000×, yielding a pixel size of 1.07 Å/pixel in counting mode. The heme-CN and 5'-pApA datasets were collected at 105,000× magnification in super-resolution mode, resulting in a final pixel size of 0.82 Å/pixel after two-fold binning. A 30° tilted dataset was also collected for the 5'-pApA sample from the same grid at the same magnification to enhance resolution.

Image Processing

All image processing steps: motion correction, contrast transfer function (CTF) estimation, particle picking, 2D classification, and 3D reconstruction were performed using CryoSPARC software package (Punjani et al., 2017).

For the apo dataset, 11,391 movies underwent patch motion correction and CTF estimation. After curation based on CTF fit resolution and ice thickness, 8,466 micrographs were retained. Initial blob picking on 500 micrographs produced 184,998 particles, extracted with a 320-pixel box size and binned to 80 pixels (4.28 Å/pixel) for computational efficiency. These underwent 2D classification into 100 classes, and 12 classes representing diverse $SmGdpP_{74}$ views were used as templates for picking across the full dataset, yielding 5,431,631 particles. After further 2D classification into 500 classes, 1,263,262 particles were re-extracted without binning (1.07 Å/pixel) and subjected to ab initio reconstruction with five classes (C1 symmetry) and heterogeneous refinement. A class containing 155,246 particles achieved a resolution of 5.48 Å, displaying clear C2 symmetry. Following reference-based motion correction and non-uniform refinement with C2 symmetry, the final map reached a resolution of 3.54 Å.

For the 5'-pApA dataset, 6,178 movies (3,072 at 0° tilt and 3,106 at 30° tilt) were collected with a pixel size of 0.82 Å/pixel. After curation, 5,131 micrographs remained for the downstream processing. Multiple rounds of particle picking and 2D classification yielded 406,214 particles, extracted with a 360-pixel box size. Ab initio reconstruction with five classes under C1 symmetry, followed by heterogeneous refinement, revealed no clear symmetry. Subsequent non-uniform refinement without symmetry constraints yielded a 3.51 Å resolution map using 86,192 particles. Focused 3D classification targeting the catalytic pocket, followed by non-uniform refinement, enhanced the resolution to 3.43 Å with 48,712 particles and improved the density of the ligand and surrounding residues.

For the heme-CN dataset, we collected 3,461 movies at a pixel size of 0.82 Å/pixel (after two-fold binning), which underwent patch motion correction and patch CTF estimation in CryoSPARC. Following multiple rounds of particle picking and 2D classification, we extracted 111,054 high-quality particles with a 360-pixel box size. These were subjected to ab initio reconstruction with two classes, followed by heterogeneous refinement. Both classes exhibited clear C2 symmetry, and subsequent non-uniform refinement with C2 symmetry applied produced a final reconstruction at 3.63 Å resolution with 67,232 particles.

Atomic Model Building and Refinement

The initial atomic models for all three structures were constructed by fitting the individual domains predicted by AlphaFold (Jumper et al., 2021) into the electron density map using UCSF Chimera (Pettersen et al., 2004). Subsequent refinements were performed using the Real Space Refinement tool from the Phenix software package (Liebschner et al., 2019), incorporating simulated annealing and morphing options. Additionally, the Coot software (Emsley et al., 2010) was used to manually refine the model, addressing Ramachandran and rotamer outliers to improve overall accuracy of the atomic models.

Phosphodiesterase Assay

$SmGdpP_{74}$ (1 μM) was incubated with 100 μM c-di-AMP in reaction buffer (10 mM Tris-HCl pH 8, 200 mM NaCl, 5 mM dithiothreitol, 1 mM $MnCl_2$) at 37°C for 5 minutes. The reaction was quenched by heating to 95°C, and precipitated protein was removed by centrifugation. The supernatant was analyzed using the coralyne assay, mixing it with 250 mM KBr and 40 μM coralyne, followed by a 10-minute incubation at room temperature (Zhou et al., 2014). The fluorescence reading for the sample (denoted as F), which represents the fluorescence intensity of the sample after the enzymatic reaction, was recorded at 475 nm emission with excitation at 420 nm using a SpectraMax i3x microplate reader (Molecular Devices, LLC). Control samples were also measured to establish baseline values: the maximum fluorescence reading (denoted as max) was obtained from a no-enzyme control sample, representing the fluorescence in the absence of hydrolysis, and the minimum fluorescence reading (denoted as min) was obtained from a no-substrate control sample, representing the background fluorescence. The percent c-di-AMP hydrolyzed was then calculated using the equation: $\left[1-\frac{F-min}{max-min}\right]\times 100$. All fluorescence measurements were performed in duplicate or triplicates to ensure reproducibility, and the calculated percent hydrolysis values were used to compare the enzymatic activity across different conditions, such as apoenzyme, heme-reconstituted, and heme-CN-reconstituted samples.

Analytical Ultracentrifugation

Sedimentation velocity analytical ultracentrifugation (SV-AUC) was conducted at 4°C using an XL-A analytical ultracentrifuge (Beckman-Coulter). Data were collected at 280 nm every 30 seconds at 15,000 RPM. Sedimentation profiles were fitted using the c(S) implementation of the Lamm equation in SEDFIT (Schuck, 2000), with coefficients corrected to standard conditions (S_{20},w). Association models were analyzed with SEDPHAT (Vistica et al., 2004), and figures were generated using GUSSI (Brautigam, 2015).

Results

$SmGdpP_{74}$ exists as functional tetramers in solution

To elucidate the molecular function of *Streptococcus mutans* GdpP (SmGdpP), we purified a truncated cytosolic construct, $SmGdpP_{74}$ (residues 74-654, theoretical molecular weight of 65 kDa for each protomer), which lacks the N-terminal transmembrane domain (Figure 1A and C). Size exclusion chromatography revealed an elution profile corresponding to a molecular mass of 239.1 kDa (Figure 1B). Sedimentation velocity analytical ultracentrifugation (SV-AUC) further corroborated this finding, showing a monodisperse 265 kDa species (Sedimentation coefficient $S_{20,w}$ = 5.95; Figure 1D). The close agreement between the methods, yielding masses approximately four-fold greater than the theoretical molecular weight, confirms that $SmGdpP_{74}$ exists a stable homotetramer in solution.

Our enzymatic characterization of $SmGdpP_{74}$ using a coralyne-based assay confirmed its catalytic activity (Figure 1E). In line with findings for the *Bacillus subtilis* GdpP homolog, reconstitution of $SmGdpP_{74}$ with heme led to strong inhibition, suppressing enzymatic activity by 74% relative to the apoenzyme (Rao et al., 2011). Notably, coordination of cyanide to heme (heme-CN) alleviated this inhibition, as also observed in *B. subtilis*, with the heme-CN-reconstituted $SmGdpP_{74}$ showing only 35% inhibition compared to the apoenzyme (Figure 1E). These results demonstrate the fine-tuned regulatory role of heme in modulating $SmGdpP_{74}$ activity. Additionally, we performed a motif search using the MEME suite on 250 GdpP homologs from genera such as *Streptococcus*, *Lactococcus*, *Enterococcus*, *Bacillus*, *Carnobacterium*, and *Dellagliola*, identifying conserved motifs (Supplementary Figure 1) that will be explored further alongside structural and functional data (Bailey et al., 2015).

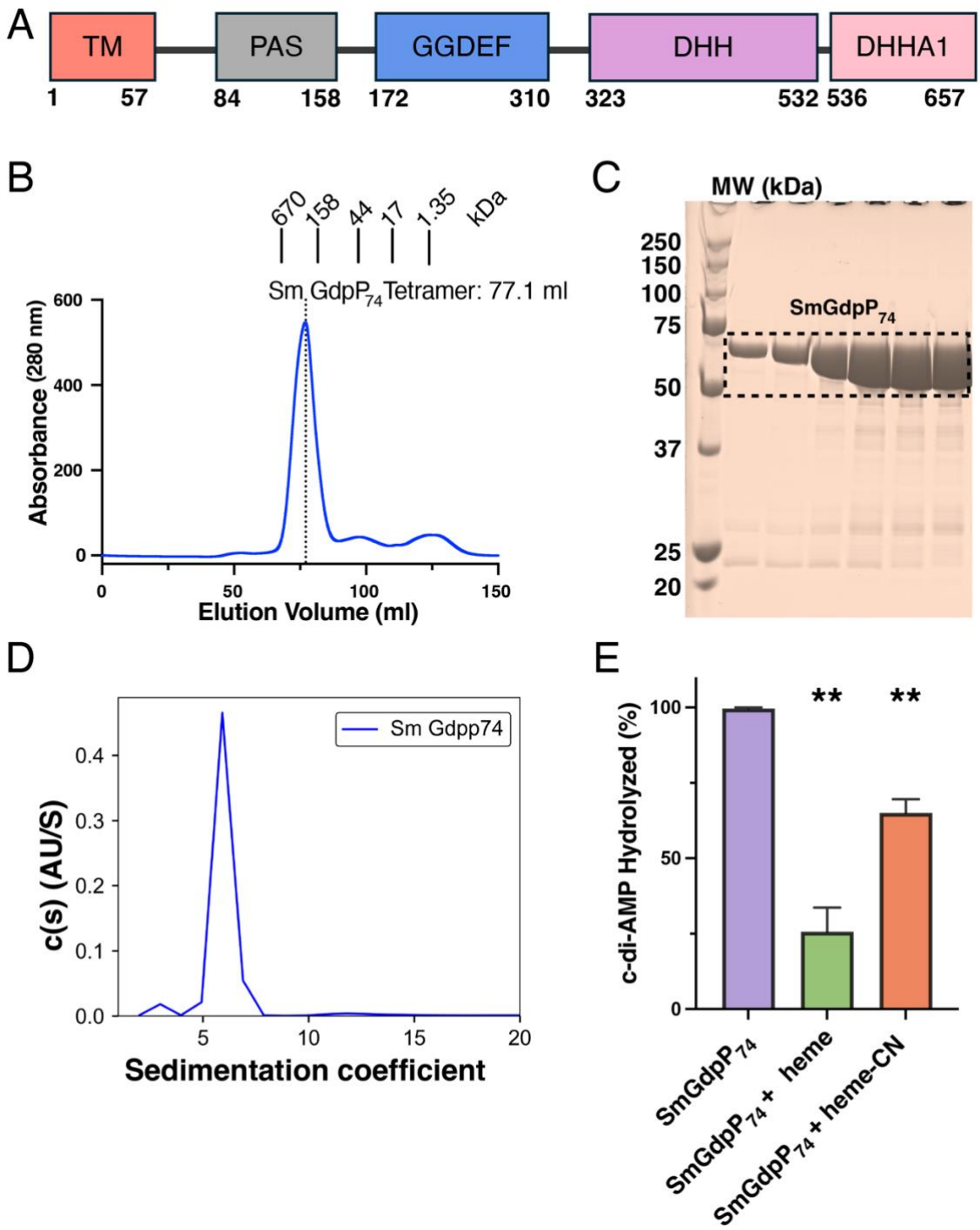

Figure 1. Domain architecture, purification, and functional characterization of SmGdpP$_{74}$. (*A*) Domain organization of full-length SmGdpP, with residue numbers indicating domain boundaries. (*B*) Size exclusion chromatography profile of SmGdpP$_{74}$. Vertical lines mark elution volumes of protein standards (labeled with molecular masses in kDa). (*C*) SDS-PAGE analysis of SEC fractions. Molecular weight markers (leftmost lane) and SmGdpP$_{74}$ bands (dashed box) are indicated. (*D*) Sedimentation velocity analytical ultracentrifugation (SV-AUC) results, showing c(S) distributions. The major peak corresponds to a molecular weight of 265 kDa (S_{20},w = 5.95). (*E*) Phosphodiesterase activity of SmGdpP$_{74}$ apoenzyme, heme-

reconstituted $SmGdpP_{74}$, and heme-CN-reconstituted $SmGdpP_{74}$ measured using the coralyne fluorescence assay. Data represent mean ± standard deviation from duplicate measurements. Significance was assessed by unpaired t-test comparing heme- and heme-CN-reconstituted samples relative to the apoenzyme (**$p < 0.01$).

Cryo-EM structure of $SmGdpP_{74}$ in apo state

To gain detailed molecular insights into the architecture of $SmGdpP_{74}$, we determined its structure using single-particle Cryo-EM at a resolution of 3.54 Å (Figure 2; Supplementary Figure 2). Consistent with the SEC and SV-AUC data (Figure 1B and D), the Cryo-EM map reveals a tetrameric assembly with C2 symmetry. Clear electron density is observed for the GGDEF, DHH, and DHHA1 domains, as well as for the linker connecting the GGDEF and DHH domains (Figure 2 A and B). However, the PAS domain exhibited high flexibility, resulting in insufficient density to construct an atomic model for this region. Local resolution across the structure varies: most of the GGDEF and DHH domains are resolved at 3 to 4 Å, whereas the local resolutions of the more flexible DHHA1 domain and linker range from 4 to 6 Å (Figure 2C and D). The overall tetrameric assembly of the $SmGdpP_{74}$ appears to be stabilized by two distinct dimerization interfaces, as shown in Figure 2E and F. The first interface is in between the GGDEF domains of chain A and B, with a buried surface area of 839 $Å^2$. The second, more extensive interface involves the DHH-DHHA1 domains of chain A and chain D on the other side, featuring a buried surface area of 1713 $Å^2$ (Figure 2F).

Heterogeneity analysis on the Cryo-EM dataset identified an additional density map that, while distinctly different from the tetrameric $SmGdpP_{74}$, closely resembles a dimeric DHH-DHHA1 fragment of the tetrameric assembly (Supplementary Figure 3). This density likely represents non-physiological degradation product arising from air-water interface (AWI) exposure and blotting stresses during grid preparations. Similar fragmentation has been commonly observed in apoferritin, hemagglutinin, and HIV-1 trimers under similar conditions (Noble et al., 2018). Such spurious fragments underscore the importance of cross-validating structural models with biophysical and functional data. The predominant tetrameric form remains the biologically relevant state, consistent with solution studies.

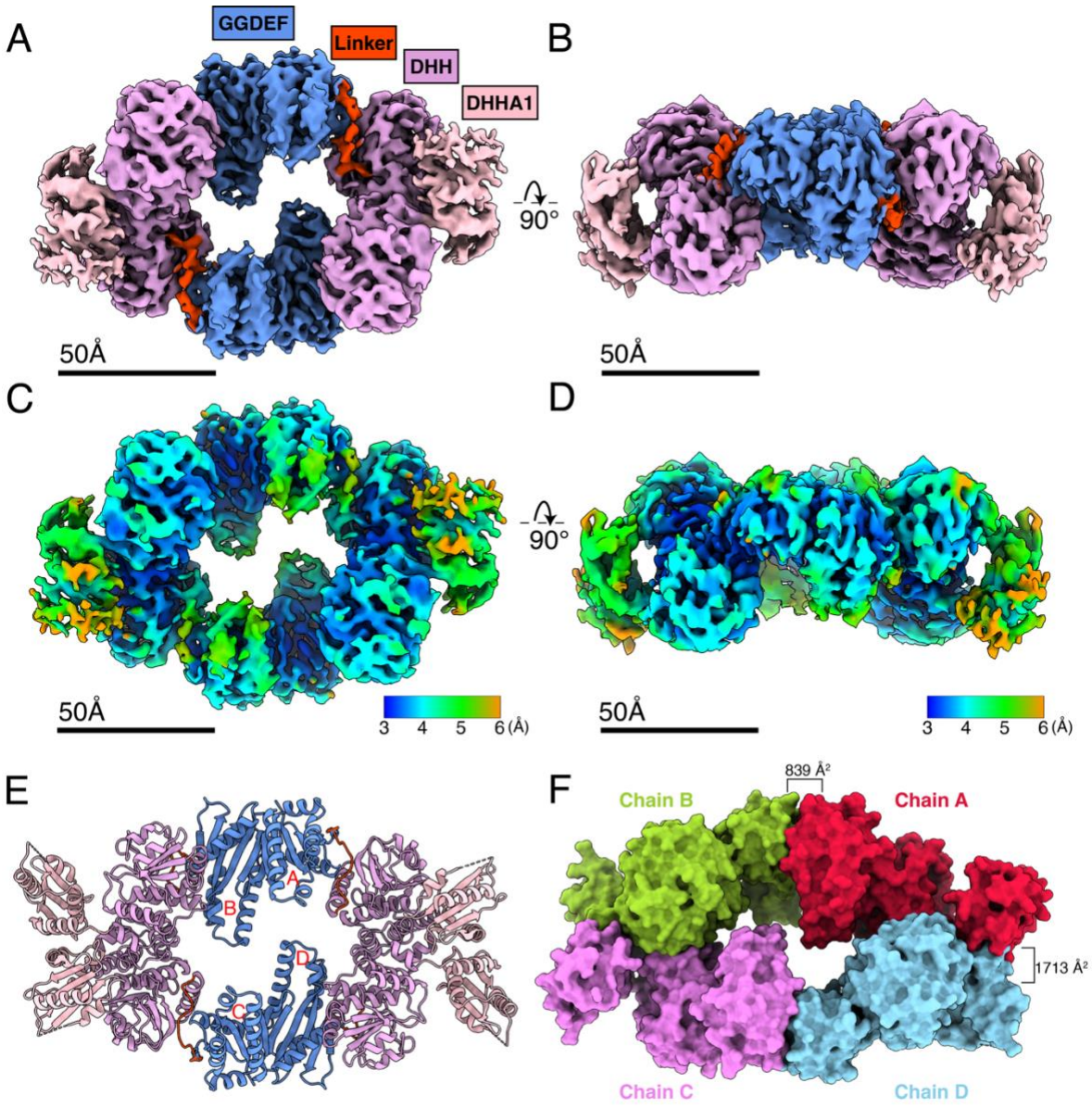

Figure 2. Cryo-EM structure of SmGdpP$_{74}$ in apo state. (*A, B*) Cryo-EM density maps (6σ contour level) of SmGdpP$_{74}$ shown in two orthogonal views, colored by domain: GGDEF (blue), linker (orange), DHH (purple), and DHHA1 (pink). (*C, D*) Local resolution estimation colored according to the resolution scale (3–6 Å). (*E*) Atomic model of the complex, with chains colored to match the domains in panels A and B. (*F*) Surface representation of the complex, highlighting individual chains (A, red; B, green; C, magenta; D, cyan) and the buried surface areas at the DHH (1713 Å^2) and GGDEF (839 Å^2) interfaces. Scale bars: 50 Å.

Our DHH-DHHA1 domain conformation analysis revealed striking structural conservation between SmGdpP$_{74}$'s DHH-DHHA1 domains and those of the *S. aureus* homolog (RMSD 0.88 Å), though one DHH domain showed a 14.9° rotational displacement along the z-

axis (Figure 3A and B). This conformational similarity suggests $SmGdpP_{74}$'s apo state adopts the same catalytically inactive arrangement observed in *S. aureus* GdpP DHH-DHHA1 domain crystal structure, where the DHH and DHHA1 domains are too distant from each other to form a catalytically active conformation (Wang et al., 2018).

We next investigated the GGDEF domain of SmGdpP (SmGGDEF), which has been characterized as "atypical" because it lacks the signature GGDEF motif essential for diguanylate cyclase activity of the canonical GGDEF domains (Rao et al., 2010). Structural comparisons with well-characterized GGDEF domains reveal that SmGGDEF domain forms a dimeric assembly that mirrors the substrate-inhibited state of the conventional GGDEF domains. Further comparison with the substrate-inhibited *T. maritima* (Tm) GGDEF domain showed that SmGGDEF domain lacks the α1 helix present in TmGGDEF (Deepthi et al., 2014; Figure 3C). Notably, while TmGGDEF bears the hallmark GGDEF motif in between the β2-β3 loop, SmGGDEF replaces this with NMDRF in this loop (Figure 3C). Intriguingly, SmGGDEF contains a conserved RGGDQ motif in its β5- α5 loop (Supplementary Figure 1, motif 2), which closely resembles the canonical GGDEF motif and could potentially be mistaken for it (Figure 3C). Structural alignment of the two GGDEF domains demonstrates high conservation in their overall folds, with the main difference being a 41.1° rotation of one SmGGDEF protomer along the z-axis relative to TmGGDEF (Figure 3D).

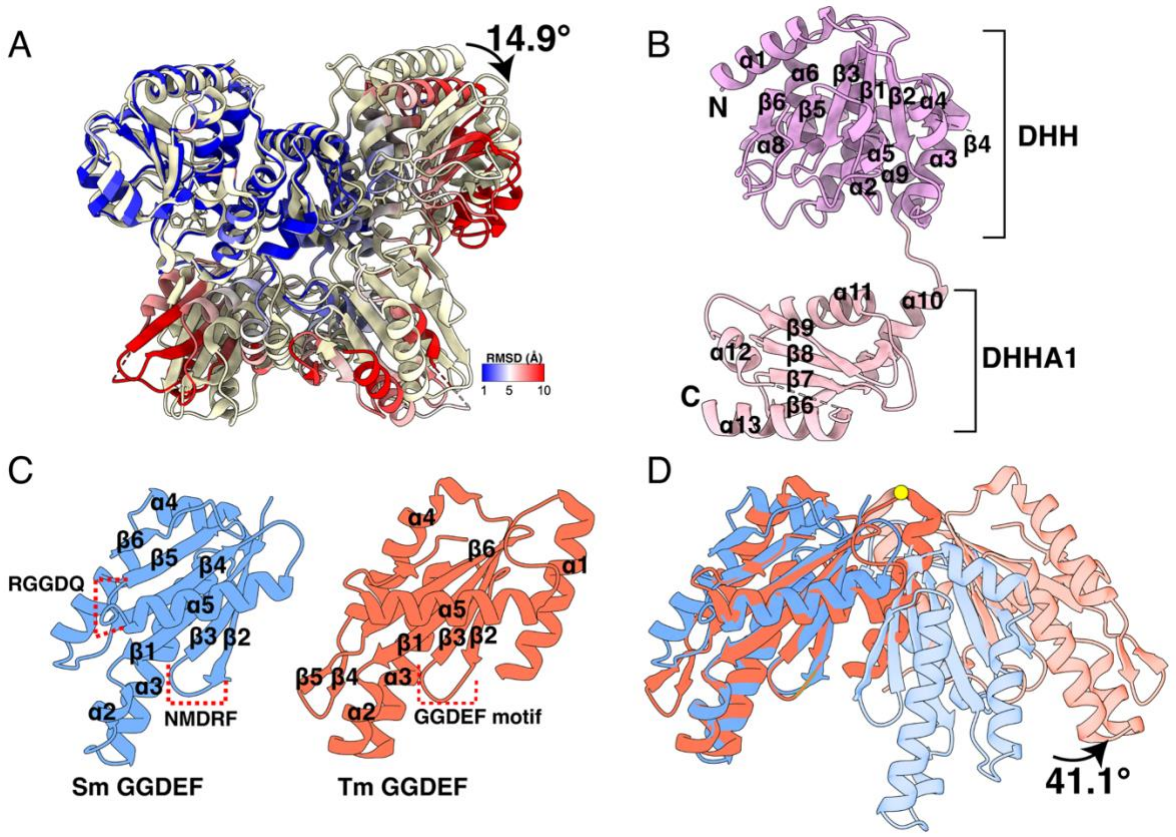

Figure 3. Structural comparison of SmGdpP GGDEF and DHH-DHHA1 domains with homologous structures. (*A*) Superposition of the SmGdpP DHH-DHHA1 dimer with *S. aureus* GdpP catalytic domain (PDB ID: 5XSI). SmGdpP DHH-DHHA1 dimer is colored by root mean square deviation (RMSD) from blue (low) to red (high), while the *S. aureus* GdpP DHH-DHHA1 dimer is shown in pale yellow. The two dimers are related by an overall RMSD of 0.88 Å across 175 pruned atom pairs. The 14.9° rotation along the z-axis is indicated. (*B*) Ribbon diagram of a single SmGdpP DHH-DHHA1 protomer, with the DHH domain in purple and the DHHA1 domain in pink. Secondary structure elements and the N- and C-termini are labeled. (*C*) Structural comparison highlighting sequence differences: SmGGDEF (left, blue) contains NMDRF sequence (β2-β3 loop) and RGGDQ motif (β5-α5 loop) compared to canonical GGDEF motif in *T. maritima* (right, orange; PDB ID: 4URS). (*D*) Superposition of the GGDEF domain dimers from SmGdpP (blue) and TmGGDEF (orange), showing a 41.1° rotation along the z-axis (indicated by a yellow dot).

Cryo-EM structure of SmGdpP$_{74}$ in the presence of heme-CN

To investigate heme-mediated inhibition of GdpP, we sought to resolve the structure of SmGdpP$_{74}$ bound to heme and heme-CN. Initial attempts with heme alone resulted in sample precipitation on the grid, but Cryo-EM analysis of the heme-CN complex yielded a 3.63 Å resolution structure (Figure 4; Supplementary Figure 4). SmGdpP$_{74}$ with heme-CN adopts a C2-symmetric tetramer, mirroring the apo structure. While the GGDEF, DHH, and DHHA1 domains were well resolved, the PAS domain exhibited only weak residual density at low contour thresholds, precluding atomic modeling (Figure 4A). Strikingly, the

two catalytic sites within each DHH-DHHA1 dimer exist in different states. One site adopts an active-like conformation, where the DHH and DHHA1 domains form a closed catalytic pocket, while the other remains in an inactive, open conformation (Figure 4D). An unidentified density was observed within each of the active-like catalytic sites (Figure 4B; Supplementary Figure 5), which superficially resembled heme with the central region of it in close vicinity of the conserved His623 residue, a hall-mark of heme-binding proteins. However, despite the possibility of incidental binding due to high heme concentrations during sample preparation, closer analysis revealed geometrical mismatches due to resolution limitations. The electron density did not fully align with the tentatively modeled heme molecule, preventing its definitive assignment (Supplementary Figure 5).

The most striking structural difference between the heme-CN and apo $SmGdpP_{74}$ forms lies in the organization of the GGDEF domains: while both structures retain dimeric configurations of chains A and B, the heme-CN structure introduces a novel interchain contact between the two diagonal chains A and C, resulting in a tetrameric assembly with a 330 $Å^2$ buried surface area at the diagonal interface (Figure 4C). This tetramerization is defined by the anti-parallel alignment of the α3 helices from diagonal GGDEF domains (Figure 4E). The assembly is stabilized by several interactions: hydrogen bonds form between D193 and Y218 at the helix ends, extensive van der Waals contacts occur along their backbones, and there is electrostatic complementarity between D193 on chain A and R219/R220 on chain C (Figure 4E and F). In contrast, the apo conformation lacks this anti-parallel helix alignment, with the α3 helices positioned far apart, evidenced by a 20.3 Å distance between D193 and Y218 and a 63.4° angle between the helices, reflecting a distinctly different quaternary arrangement.

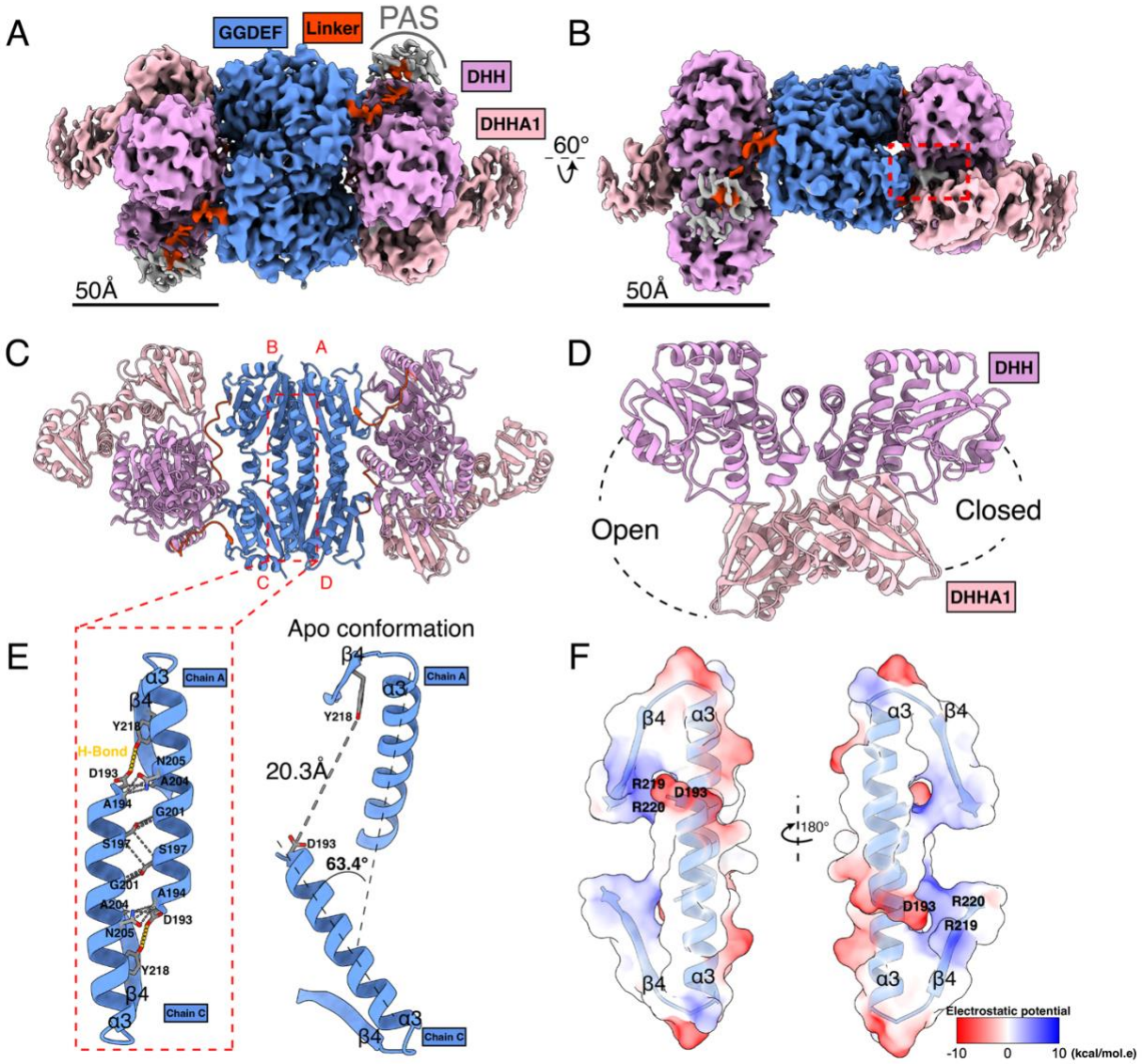

Figure 4. Cryo-EM structure of SmGdpP$_{74}$ in the presence of heme-CN. (*A, B*) Cryo-EM density maps of the SmGdpP$_{74}$ tetramer in heme-CN conformation, related by a 60° rotation along the x-axis. Domains are colored as indicated: PAS (gray), GGDEF (blue), linker (orange), DHH (purple), and DHHA1 (pink). The unidentified density (shown in gray) in the catalytic pocket is highlighted with red dashed box in panel B. (*C*) Atomic model of the tetramer, highlighting chains A–D and the novel interchain interface (red dashed box) formed between chains A and C. (*D*) Ribbon diagram of a DHH-DHHA1 dimer. (*E*) Novel anti-parallel α3 helix interface between chains A and C in the heme-CN structure (left), stabilized by hydrogen bonds (yellow dashed lines) between D193 and Y218, and comparison to the apo conformation (right), where the α3 helices are separated by 20.3 Å and oriented at a 63.4° angle. Van der Waals interactions between residues on chains A and C are highlighted with gray dashed lines (left). (*F*) Electrostatic surface representation of the α3–β4 interface, showing electrostatic complementarity and key residues (D193, R219, R220). Scale bars: 50 Å.

Post-catalytic Cryo-EM structure of SmGdpP$_{74}$ complexed with 5'-pApA

Cryo-EM analysis of $SmGdpP_{74}$ incubated with excess c-di-AMP under manganese-depleted conditions yielded an initial 3D reconstruction, featuring a well-resolved GGDEF domain tetramer and a single DHH-DHHA1 dimer. The second DHH-DHHA1 dimer exhibited poor resolvability, revealing an asymmetric architectural arrangement (Figure 5A and B; Supplementary Figure 6E and F). To address this asymmetry, 3D reconstruction was performed without applied symmetry, achieving a final reconstructed map at 3.43 Å overall resolution (Supplementary Figure 6). Local resolution (Figure 5B) varied across the structure: most of the GGDEF tetramer and one DHH-DHHA1 protomer resolved at 3-4 Å, while the less-defined DHH-DHHA1 protomer displayed lower resolution (4-6 Å). Our methodological shift to asymmetric reconstruction enabled capture of this native conformational ensemble, bypassing artifacts introduced by imposed symmetry averaging.

Cryo-EM analysis revealed asymmetric ligand occupancy in the catalytic pockets of $SmGdpP_{74}$, with one pocket containing distinct electron density while the other remained unoccupied. Focused 3D classification identified the density as 5'-pApA, the linear hydrolysis product of c-di-AMP, rather than the intact cyclic dinucleotide (Figure 5C and D). This conclusion was based on the absence of phosphodiester bond continuity, a diagnostic feature distinguishing hydrolyzed products from substrates in HD-domain phosphodiesterases (Huynh et al., 2015). This finding suggests that the structure represents the post-catalytic conformation $SmGdpP_{74}$. The 5'-pApA adopts a conformation similar to c-di-AMP, except for its 5'-phosphate moiety, which is oriented toward the DHH domain (Figure 5D). Structurally, 5'-pApA forms hydrogen bonds with residues D350, S602, and S573. Additionally, it engages in van der Waals interactions: G620 and G622 interact with the adenine base of 5'-pApA, while A627 interacts with the ribose moieties. Despite resolution limitations precluding modeling of catalytic water molecules or Mn^{2+} ions, the structure aligns with hydrolysis mechanisms proposed for DHH-DHHA1 domain containing enzymes, where metal-coordinated nucleophilic water cleaves phosphodiester bonds (He et al., 2016; Wang et al., 2018).

A structural similarity search of the DHH-DHHA1 domains of $SmGdpP_{74}$ bound to 5'-pApA against the PDB database uncovered a striking resemblance to Mtb DhhP (Rv2837c; PDB ID: 5JJU) also complexed with 5'-pApA (Figure 5E; He et al., 2016). The structural resemblance is quantified with an RMSD value of just 1.26 Å across 128 pruned atom pairs. The key distinction between these structures lies in the orientation of 5'-pApA. In the $SmGdpP_{74}$-pApA complex, the PO_3 moiety of 5'-pApA is directed toward the DHH domain, indicative of a post-catalytic conformation. Conversely, in the DhhP crystal structure, 5'-pApA is flipped with the PO_3 moiety pointing down towards the DHHA1 domain, with the phosphodiester bond positioned near the binuclear metal center of the DHH domain, reflecting a pre-catalytic state poised for hydrolysis of 5'-pApA to AMP (Figure 5E). It has been proposed that GdpP cannot further hydrolyze 5'-pApA to AMP

due to its inability to facilitate internal flipping of 5'-pApA, a process hindered by steric constraints within its active site (Wang et al., 2018). This structural limitation underscores a critical functional divergence among DHH-DHHA1 phosphodiesterases, highlighting how subtle differences in active site architecture can profoundly impact catalytic outcomes in bacterial second messenger metabolism.

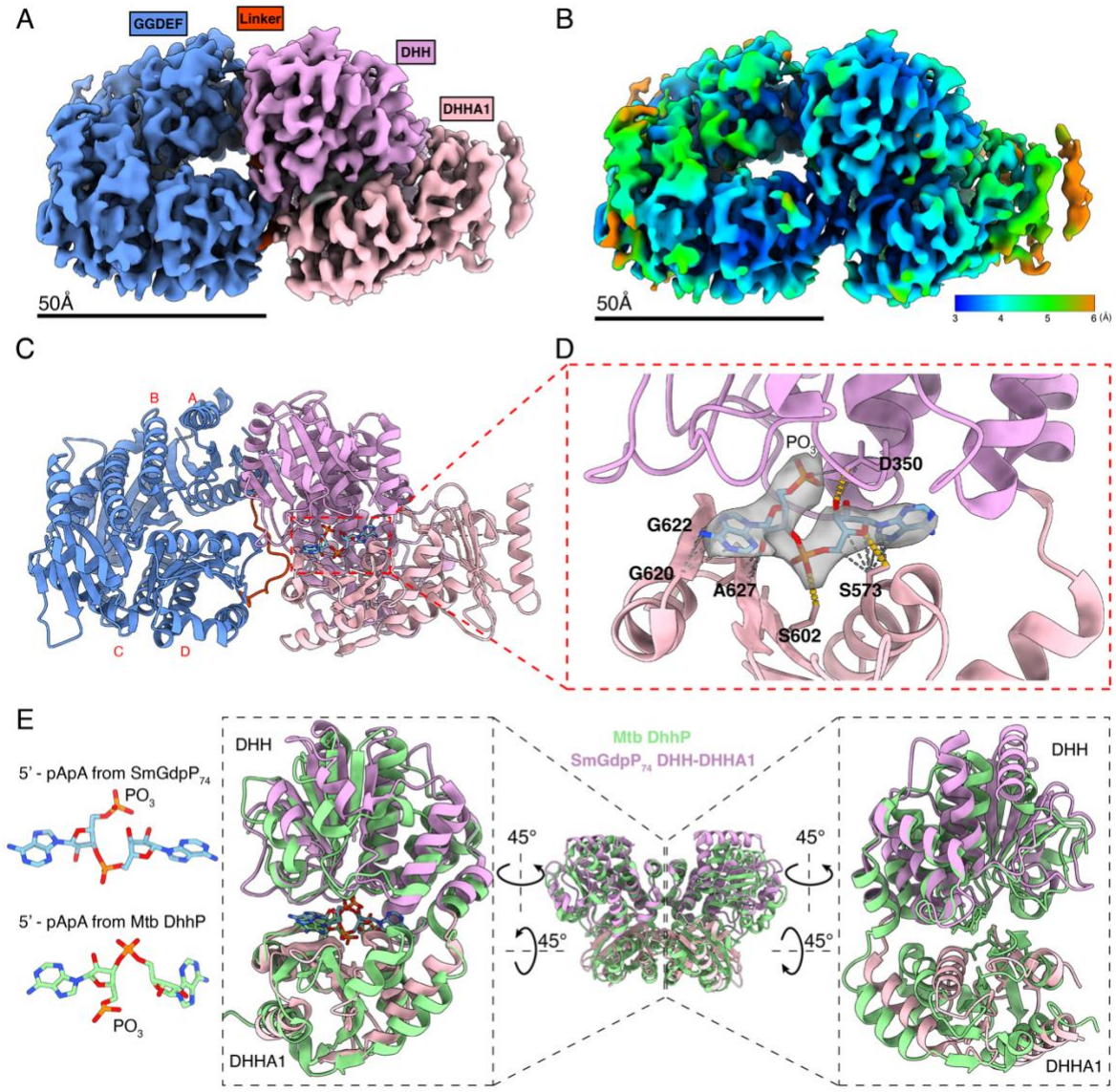

Figure 5. Cryo-EM structure of SmGdpP$_{74}$ in complex with the linear hydrolysis product 5'-pApA. (*A*) Cryo-EM density map of the SmGdpP$_{74}$ tetramer, colored by domain: GGDEF (blue), linker (orange), DHH (purple), and DHHA1 (pink). (*B*) Local resolution estimation of the Cryo-EM map, colored according to the resolution scale shown in Å. (*C*) Atomic model of the SmGdpP$_{74}$ tetramer, with chains A–D labeled and the bound 5'-pApA molecule highlighted at the DHH-DHHA1 active site (red dashed box). (*D*) DHH-DHHA1 active site details showing 5'-pApA (cyan) inside the electron density (gray mesh, 12 σ contour). Hydrogen bonds (yellow dashed lines) are formed between 5'-pApA and residues D350, S602, and S573,

while van der Waals interactions are observed with S573, G620, G622, and A627. (*E*) Structural superposition of Mtb DhhP (green; PDB ID: 5JJU) and $SmGdpP_{74}$ DHH-DHHA1 domains (purple/pink) in the center, with enlarged views of the left and right protomers shown at 45-degree rotations along the x- and y-axes. Adjacent insets (left) display the 5'-pApA conformations with PO_3 moiety labeled, as bound in $SmGdpP_{74}$ (top) and Mtb DhhP (bottom). Scale bars: 50 Å.

GGDEF domain scaffolds the active conformation of the DHH-DHHA1 domain of $SmGdpP_{74}$

A detailed structural analysis of $SmGdpP_{74}$ with 5'-pApA reveals a unique interdomain architecture in which two GGDEF domains scaffold the catalytic DHH-DHHA1 domain at opposite ends (Figure 6A). At one end, the GGDEF domain from chain D interacts with the DHHA1 domain of the same chain through the initial portion of the linker. At the other end, the GGDEF domain from chain A engages both the α1 helix of the chain D DHH domain and the C-terminal region of the linker, including residues R319, S320, and R321. These inter-chain interactions are stabilized by an extensive hydrogen-bonding network involving key conserved residues: D293 from the RGGDQA segment of motif 2 and N183 from the DNYDD segment of motif 1 (Supplementary Figure 1) in chain A GGDEF form hydrogen bonds and electrostatic contacts with R325 and T322 of the chain D DHH domain, respectively. The functional importance of these contacts is underscored by mutagenesis studies, as substitutions such as D182R/N183R (motif 1) and D293R (motif 2) severely diminish c-di-AMP hydrolysis activity to less than 25% of wild-type levels (Figure 6B). Additional stabilization is provided by L288 and N285 from chain A GGDEF, which form hydrogen bonds with the R319S320R321 segment of the chain D linker, effectively bridging the two GGDEF domains. Furthermore, R290 and G311 from chain D GGDEF establish hydrogen bonds with R447 (chain D DHH), as well as E616 and N610 (both in the DHHA1 domain of chain D), creating a dense network of interactions around the 5'-pApA-bound active site. To further probe the functional relevance of the tetrameric GGDEF assembly, the R219D/R220D double mutant was introduced to disrupt electrostatic interactions between the diagonal GGDEF domains (chains A and C; Figures 6A, 4E, and 4F), resulting in a drastic reduction of phosphodiesterase activity to just 8% of wild-type levels (Figure 6B). Collectively, this intricate scaffolding arrangement is anchored by conserved motif residues, stabilized through precise hydrogen-bond and electrostatic interactions. This architecture is essential for maintaining the proper orientation and stability of the catalytic DHH-DHHA1 domains, thereby ensuring efficient substrate processing.

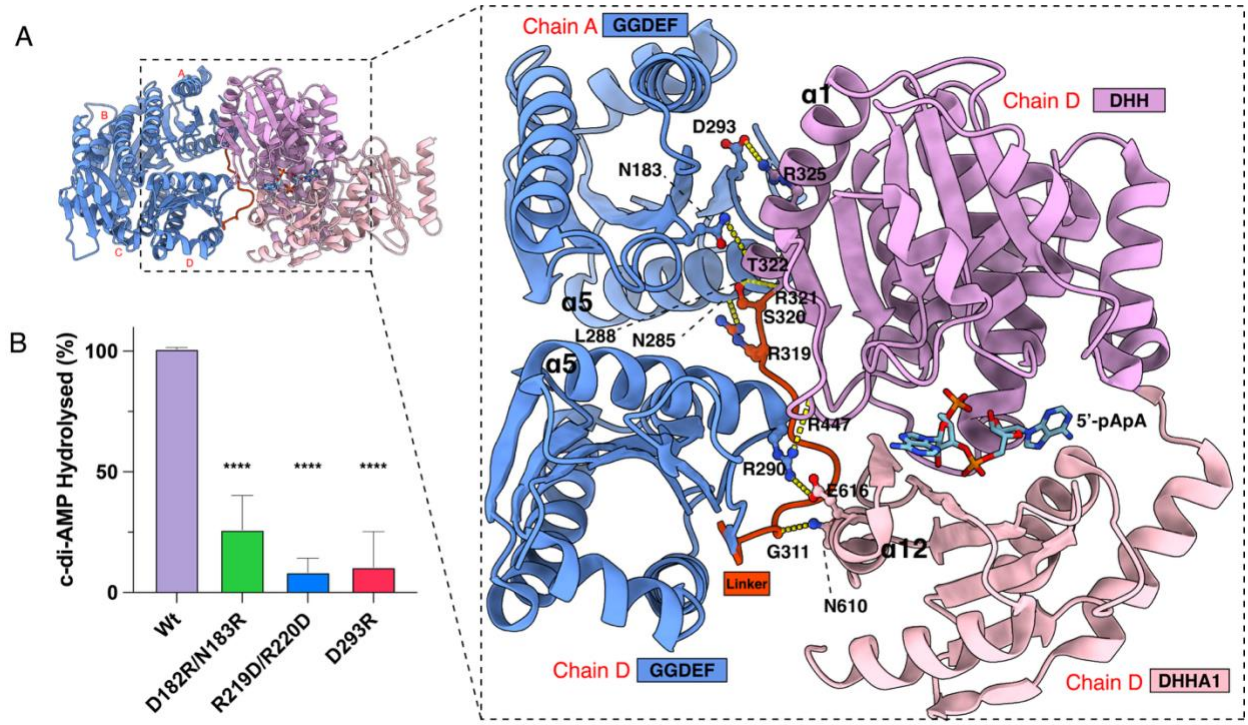

Figure 6. Interdomain interactions between GGDEF and DHH-DHHA1 domains in 5'-pApA bound active conformation. (*A*) Structural overview (left) and detailed interaction map (right) showing the GGDEF domain (blue) and DHH-DHHA1 domains (purple/pink). Hydrogen bonds are depicted as yellow dashed lines, with the interacting residues labeled. Side chains involved in hydrogen bonding are shown in ball-and-stick representation. Key interactions: D293 (RGGDQA motif) and N183 (DNYDD motif) from chain A GGDEF contact R325/T322 of chain D DHH; L288/N285 bridge to R319-S320-R321 linker segment. For main chain hydrogen bonding residues (N285, L288, R447), side chains are not displayed. (*B*) Relative phosphodiesterase activity of the three GGDEF domain mutants compared to wild-type (normalized to 100%). Data represent mean ± standard deviation from two sets of triplicate measurements. Statistical significance is indicated by asterisks (****$p < 0.0001$).

Structural comparison reveals conformation landscape for DHH-DHHA1 domains

Comparative analysis of $SmGdpP_{74}$ in the 5'-pApA-bound and heme-CN states revealed conserved GGDEF domain architecture (RMSD 0.6 Å, 116 atoms pruned), with tetrameric assemblies maintaining near-identical geometry (Figure 7A and B). However, ligand-specific rearrangements occurred in the DHH-DHHA1 domains: both protomers adopted closed configurations in the 5'-pApA structure (Figure 7C and D), contrasting with the partial closure observed in the heme-CN conformation. Our quantitative assessment of DHH-DHHA1 domain closure utilized intramolecular distances between conserved catalytic residues D350 (DHH subdomain) and S602 (DHHA1 subdomain), which coordinate 5'-pApA via hydrogen bonding in the $SmGdpP_{74}$-pApA complex structure (Figure 5D). This analysis revealed three distinct conformational states (Figure 7E): an 'active' state at 10.5 Å (5'-pApA protomer 1); an 'active-like' state at ~15 Å (5'-pApA protomer 2, heme-CN protomer 1); and an 'inactive' state spanning 18–21 Å (heme-CN

protomer 2, apo forms, *S. aureus* GdpP catalytic domain). This landscape of DHH-DHHA1 domain conformations suggest ligand binding induces progressive domain closure, with complete active-site compaction requiring specific substrate or product interactions. The conserved GGDEF architecture likely stabilizes the tetrameric scaffold during these rearrangements, while DHH-DHHA1 mobility enables allosteric modulation, a mechanism consistent with cyclic nucleotide signaling pathways.

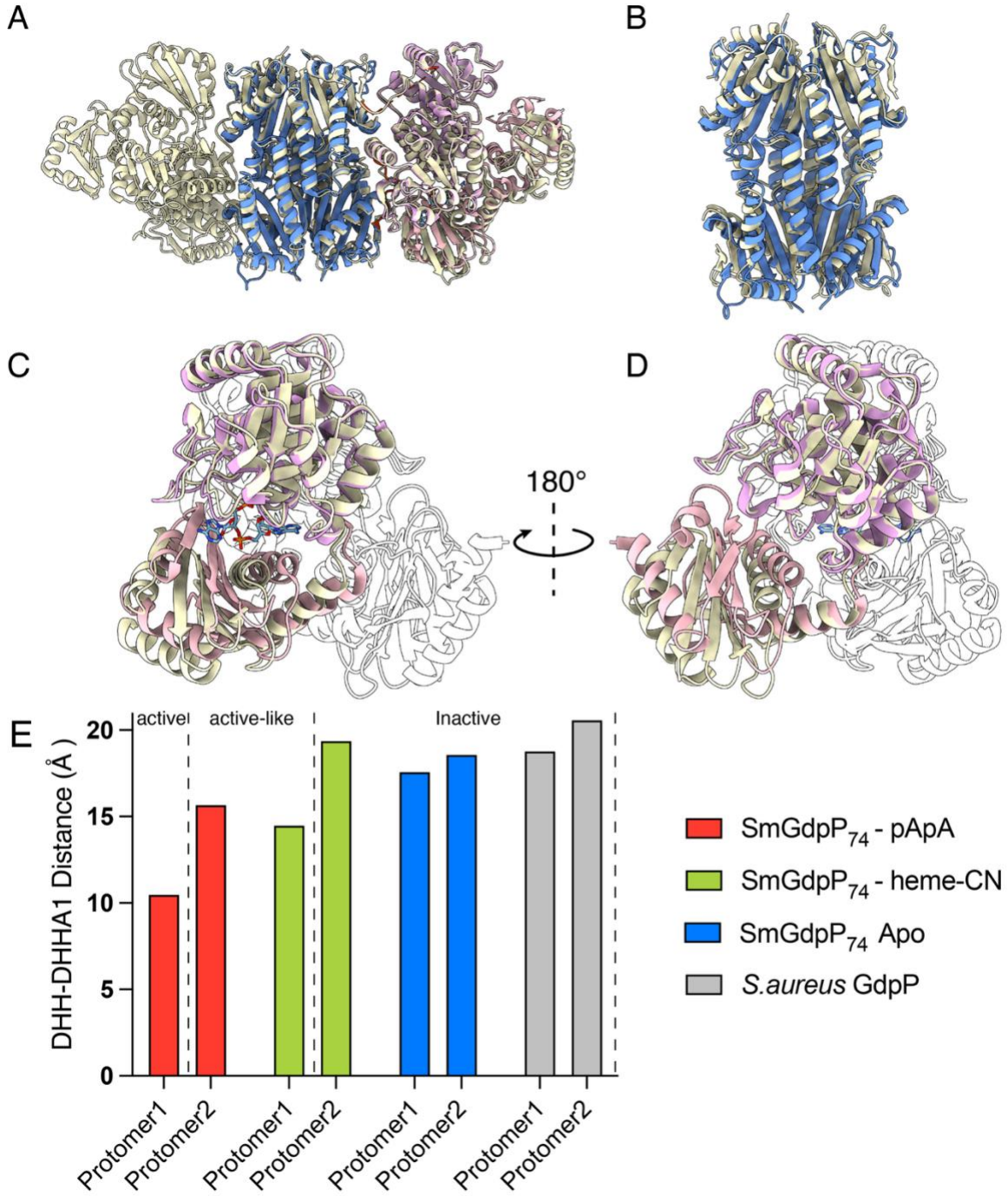

Figure 7. Comparative structural analysis of SmGdpP$_{74}$ in 5'-pApA-bound conformation with heme-CN conformation. (*A, B*) Structural superposition of SmGdpP$_{74}$ tetramers in pApA-bound, colored by domain: GGDEF (blue), DHH (purple), DHHA1 (pink), and heme-CN (yellow) states. (*C, D*) DHH-DHHA1 dimer conformations in 5'-pApA-bound (purple/pink) and heme-CN (yellow) structures, shown in two orientations related by 180° rotation. (E) Quantitative conformational analysis of DHH-DHHA1 domain closure measured using distances between Cα atoms of residues D350 and S602. Three distinct states identified: 'active' (≤11 Å); 'active-like' (13-16 Å); and 'inactive' (≥18 Å). Different conformational states are marked by vertical dashed lines.

Structural comparisons between the apo and heme-CN conformations of SmGdpP[74] reveal extensive domain reconfigurations mediated by flexible interdomain linkers (Figure 8A and B). Major differences between the two structures involve rotations of the DHH-DHHA1 domains relative to the GGDEF domains. More specifically, with top GGDEF dimers aligned (Figure 8C), the right DHH-DHHA1 dimers of the apo conformation undergo a 94° rotation coupled with a 9.6 Å translational shift when transitioning between states, while its left DHH-DHHA1 dimers reposition via a 66° rotation and 4.4 Å translation. Similarly, the bottom GGDEF dimer of the apo conformation exhibits a 66° rotational adjustment accompanied by 4.7 Å translational movement with top GGDEF dimers aligned (Figure 8C). These coordinated rigid-body displacements, visualized through morphing trajectories (Video 1), highlight the critical role of linker flexibility in facilitating large-scale structural transitions without compromising the conserved architecture of the GGDEF tetrameric scaffold. The observed motions suggest a unidirectional allosteric mechanism where stable GGDEF domains enable ligand-induced repositioning of DHH-DHHA1 domains.

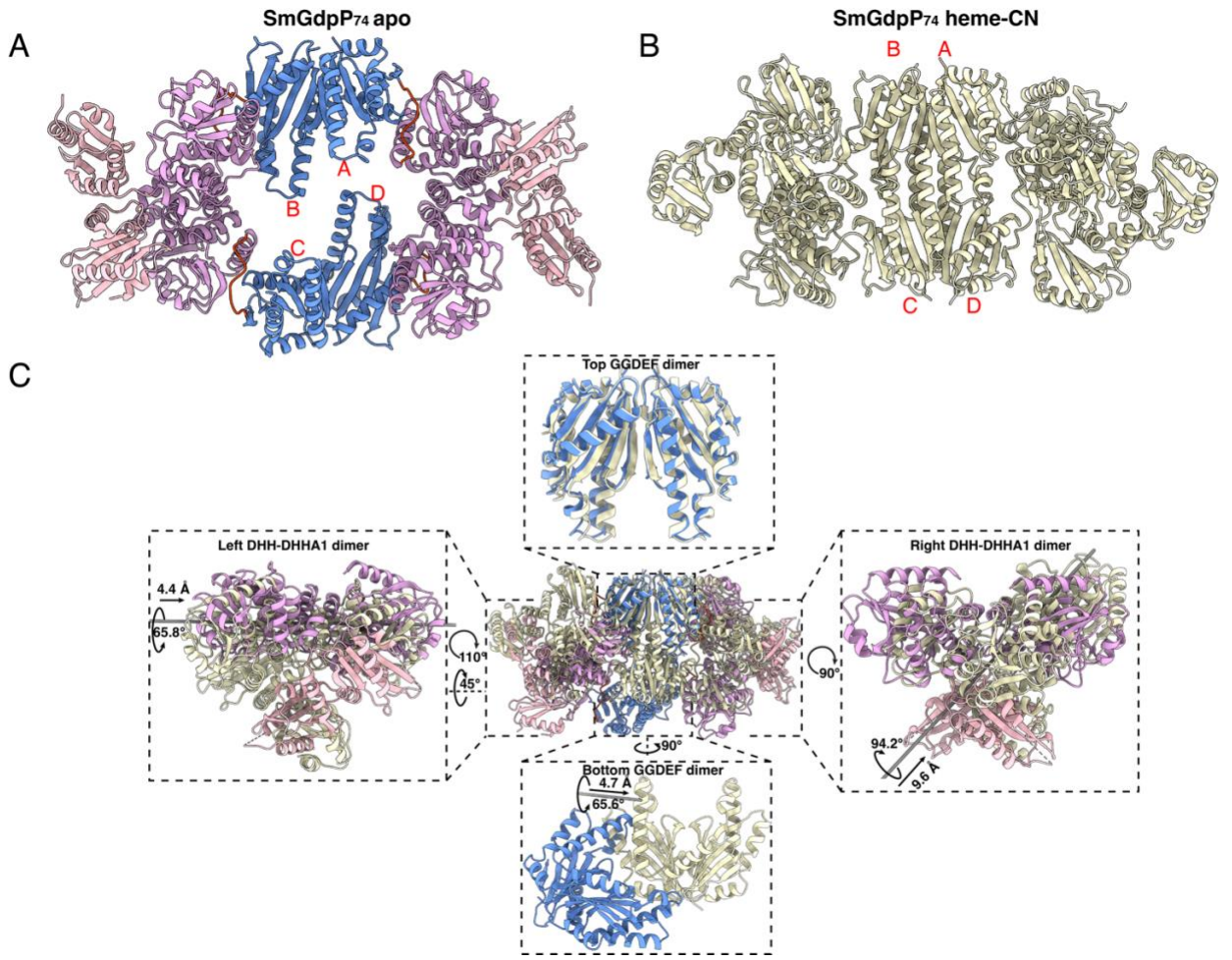

Figure 8. Structural comparison of SmGdpP$_{74}$ tetramers in apo and heme-CN conformations. (*A*) Ribbon representation of the apo SmGdpP$_{74}$ tetramer, colored by domain: GGDEF (blue), DHH (purple), and DHHA1 (pink), with chains A–D labeled in red. (*B*) Ribbon representation of the heme-CN-bound SmGdpP$_{74}$ tetramer, uniformly colored pale yellow, with chains A–D labeled in red. *(C)* Structural superposition of SmGdpP$_{74}$ tetramers in apo (domain-colored) and heme-CN (pale yellow) conformations, aligned based on optimal superposition of the top GGDEF dimers (chains A-B). Conformational changes are quantified through rigid-body analysis measuring rotational and translational displacements relative to the aligned reference frame. Three insets highlight domain-specific rearrangements, showing the bottom GGDEF dimer rotating 65.6° with a 4.7 Å translation along the indicated axis (gray line), the left DHH-DHHA1 dimer rotating 65.8° with a 4.4 Å displacement, and the right DHH-DHHA1 dimer demonstrating the most extensive change with a 94.2° rotation and a 9.6 Å translation. Rotation axes and translation vectors are indicated by gray lines, with the morphing trajectory between conformations visualized in Video 1.

The GGDEF-DHH Linker Governs SmGdpP$_{74}$ Allostery

The GGDEF-DHH linker region of SmGdpP$_{74}$ contains part of conserved motif 3 (Supplementary Figure 1), spanning residues G310 to R321 (Figure 9A). Cryo-EM

structures of $SmGdpP_{74}$ in both apo and heme-CN states revealed that this linker serves as a flexible hinge, mediating large-scale rotations and translations of the DHH-DHHA1 domains relative to the GGDEF scaffold (Figure 8A–C; Video 1). The linker is strategically positioned to transmit conformational changes triggered by ligand binding, and its flexibility appears essential for the dynamic interdomain rearrangements observed during allosteric transitions. Therefore, we sought to dissect the role of the linker in $SmGdpP_{74}$ allosteric regulation.

Conserved glycine residues enable linker flexibility

To experimentally probe the functional importance of linker flexibility, we first targeted the N-terminal glycine residues (G310 and G311), which are predicted to impart backbone pliability. Mutating both glycines to alanines (GG310AA) resulted in a 28% reduction in c-di-AMP hydrolysis activity, while substitutions to bulkier residues—valine (GG310VV), leucine (GG310LL), and proline (GG310PP)—caused more severe defects, with GG310VV exhibiting a dramatic 93% loss of function (Figure 9B). This could be attributed to valine's branched side chain at the Cβ position restricting backbone φ/ψ flexibility. These findings underscore the critical role of glycine-mediated flexibility in facilitating the large-scale domain movements required for substrate hydrolysis, consistent with the idea that linker rigidity can restrict the conformational ensemble accessible to the enzyme.

KRSR motif as a critical allosteric switch

In the heme-CN structure, density map analysis uncovered a weakly resolved density above the linker and the α1 helix of the DHH domain. This likely corresponds to the PAS domain, which suggests significant direct interaction between the PAS and DHH domains with the linker positioned between them (Figure 9C). This observation implies that the conserved residues on the linker, beginning with the K318-R321 (KRSR) motif, may play a crucial role in relaying inhibitory signals from the PAS domain to the DHH domain (Figure 9C).To test this, we generated the KRSR/GAGA (K318-R321 to GAGA) mutant and compared its activity to wild-type and other linker mutants, TRTR/GAGA (T322-R325 to GAGA) and AMM/GAA (A326-M328 to GAA). The mutant proteins were incubated with a 5-fold excess of heme prior to size-exclusion chromatography to ensure heme reconstitution (Supplementary Figure S7), and their activities were compared to the wild-type enzyme with and without heme (Figure 9D). Remarkably, although all mutants maintained baseline activities, only the KRSR/GAGA mutant completely lost heme-mediated inhibition (Figure 9D), identifying this motif as the critical node for PAS domain inhibition of phosphodiesterase activity. This discovery highlights the KRSR motif as a vital molecular switch in regulating GdpP activity through allosteric mechanisms, likely by

stabilizing the interactions between the PAS and DHH domains, and positions it as a promising target for disrupting heme-dependent GdpP inhibition in Firmicutes.

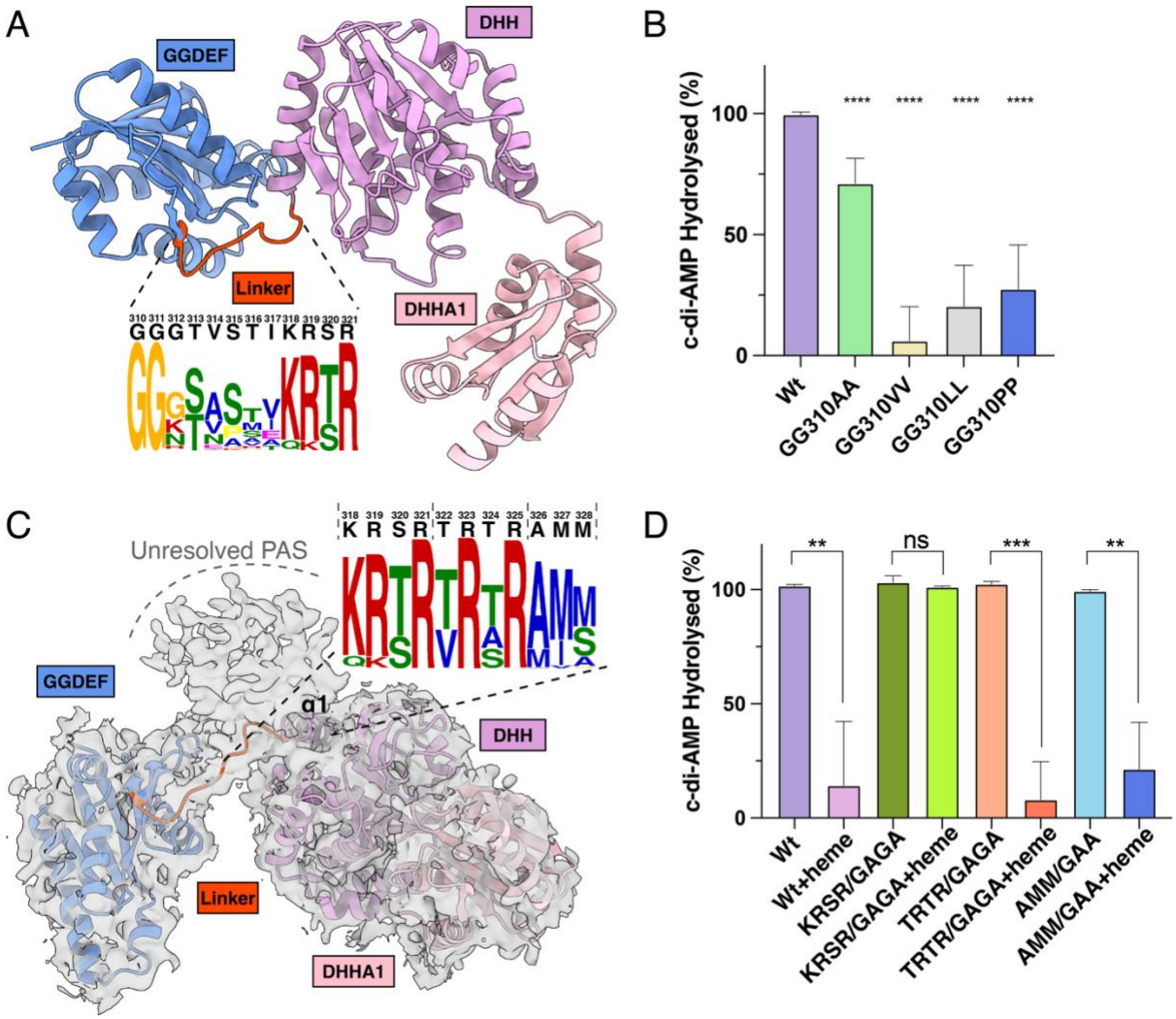

Figure 9. Conserved motif residues in the GGDEF-DHH linker of SmGdpP$_{74}$ and effects of targeted mutagenesis. (*A*) Structure of a single SmGdpP$_{74}$ protomer in the apo conformation, with domains colored as indicated: GGDEF (blue), DHH (purple), and DHHA1 (pink). The GGDEF-DHH linker is highlighted in orange, and linker residues G310–R321 are shown in black with their residue numbers. The sequence logo below depicts the conserved motif within this linker region. (B) Relative c-di-AMP hydrolysis activity of glycine mutants normalized to wild-type (100%). Progressive flexibility reduction correlates with activity loss: GG310AA (72% activity), GG310VV (7% activity), GG310LL (15% activity), GG310PP (25% activity). Data represent mean ± standard deviation from triplicate independent experiments. (*C*) Structure of a single SmGdpP$_{74}$ protomer in the heme-CN conformation, shown within the electron density map. The unresolved PAS domain is indicated by dashed lines. The linker region and the start of the α1 helix in the DHH domain are highlighted, with conserved residues K318–M328 shown in black. The corresponding sequence motif is displayed below, with dashed lines marking the regions mutated in panel D. (D) Pairwise comparison of heme-mediated inhibition across linker mutants. All proteins pre-incubated with 5-fold molar excess heme

and purified by SEC to ensure reconstitution (Supplementary Figure 7). Statistical significance is indicated as follows: **p < 0.01; ***p < 0.001; ****p < 0.0001; ns, not significant.

Mutational analysis reveals DHHA1 interface is crucial for asymmetric catalysis

Building upon the findings of Wang et al. (2018), who identified critical catalytic residues in the DHH-DHHA1 domains of *S. aureus* GdpP, we conducted a comprehensive mutational analysis of previously unexplored active site residues in $SmGdpP_{74}$. Our investigation targeted five active site residues (D384A, H445A, L498A, K501A, and N569A) and several key residues at the dimerization interfaces of both the DHH and DHHA1 domains (Figure 10). Among these, D384A, H445A, and L498A exhibited moderate reductions in catalytic activity, while K501A resulted in the most pronounced loss of function, suggesting its critical role in substrate coordination or catalysis. Conversely, the N569A mutation maintained activity comparable to wild-type levels, indicating this residue may play a peripheral role in the catalytic mechanism (Figure 10B).

To further investigate the structural basis of catalysis, we examined the dimerization interfaces within both the DHH and DHHA1 domains by targeting conserved residues on the respective α8 and α10 helices (Figure 10 C and D). Remarkably, mutations in the DHH domain interface (the triple mutants T508A/S509A/R510D and T511A/F512A/D513R) showed minor or negligible effects on enzymatic activity, demonstrating considerable tolerance to structural perturbations at this interface (Figure 10 B and C). In stark contrast, disruption of the DHHA1 domain's α10 helix dimerization interface through double mutations (D535R/F536A and Y539A/R540D) led to substantial decreases in enzymatic activity, highlighting the critical importance of this interface for maintaining catalytic function (Figure 10 B and D). As a control, we introduced the D537R/E538R double mutation targeting residues located on the α10 helix but outside the dimerization interface (Figure 10D), which preserved wild-type activity levels, confirming the specificity of our findings.

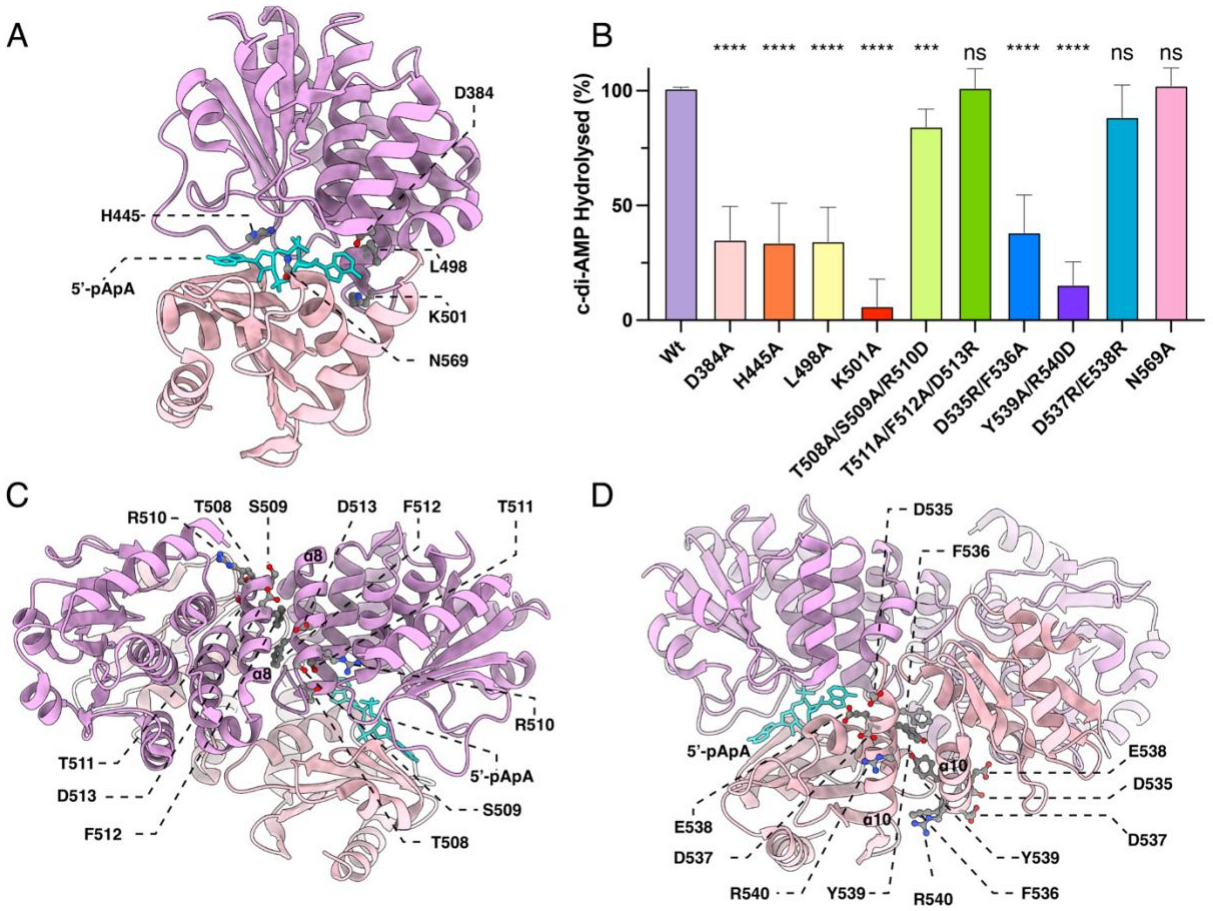

Figure 10. Systematic mutagenesis analysis of DHH-DHHA1 active site and dimerization interfaces based on structural analysis and sequence conservation. (*A*) Structural overview of the DHH-DHHA1 domains bound to 5'-pApA (cyan), highlighting five previously uncharacterized active site residues (D384, H445, L498, K501, N569) targeted for mutagenesis. (*B*) Relative phosphodiesterase activity of the mutant proteins compared to the wild-type. Active site mutants: D384A (35%), H445A (33.5%), L498A (34.2%), K501A (5.9%), N569A (102.1%). DHH interface mutants retain high activity: T508A/S509A/R510D (84.2%), T511A/F512A/D513R (101%). DHHA1 interface disruption severely reduces activity: D535R/F536A (38.1%), Y539A/R540D (15.3%). Data normalized to wild-type; mean ± standard deviation from two sets of triplicate experiments. (*C*) Structure of the DHH domain dimerization interface is shown, with the α8 helices and key mutated residues (T508, S509, R510, T511, F512, D513) labeled. (*D*) Structure of the DHHA1 domain dimerization interface highlights the α10 helices and residues targeted for mutagenesis (D535, F536, Y539, R540, D537, E538).

Modeling full-length SmGdpP in a membrane mimic reveals ligand-dependent re-organization of the transmembrane bundle

To place the Cryo-EM reconstructions of $SmGdpP_{74}$ in the context of the intact, membrane-anchored enzyme, AlphaFold server was used to predict full-length SmGdpP structure in the presence of 50 oleic-acid molecules as membrane mimics (Jumper et al.,

2021). As anticipated, the oleic acid molecules encircle the transmembrane region of SmGdpP, forming a quasi-membrane environment (Figure S8 A, D). Remarkably, these predicted structures show a high-degree of similarity to our Cryo-EM structures of $SmGdpP_{74}$ in both apo and heme-CN conformation, confirming that the truncated constructs faithfully capture the conformational states of the full-length protein. In the apo-like model, the TM helices are nearly colinear and extend straight through the membrane, positioning the cytosolic tetramer distant from the bilayer surface (Figure S8 A, B, C). In contrast, when adopting a conformation akin to the heme-CN state, characterized by the antiparallel stacking of α3 helices in diagonal GGDEF domains, the transmembrane region shifts to a more compact, membrane proximal arrangement (Figure S8 D, E, F). These ligand-dependent movements indicate that the large-scale rearrangements observed in the cytosolic domains are likely to be mechanically coupled to the TM helices, providing a plausible route for signal propagation across the membrane. In this context, SmGdpP allostery is likely not confined to intracellular regulation of c-di-AMP hydrolysis but also modulates membrane-associated processes, offering new avenues to probe how environmental cues sensed by the PAS domain influence bacterial physiology and pathogenesis.

Discussion

DHH-DHHA1 asymmetric catalytic coupling

Our structural analysis of $SmGdpP_{74}$ structures using intramolecular distances between conserved DHH-DHHA1 domain catalytic residues identifies three distinct conformational states: 'active' (~10.5 Å), 'active-like' (~15 Å), and 'inactive' (18-21 Å), demonstrating that the enzyme samples multiple conformations. In all of the structures, one DHH-DHHA1 protomer adopts a more closed, catalytically poised conformation than its partner, revealing an intrinsic asymmetry at the dimeric interface. Similar asymmetric conformational heterogeneity is observed in other DHH-DHHA1 family proteins, including NrnA and RecJ exonucleases, where the DHHA1 domains exhibits high mobility and differential conformational states between protomers (Schmier et al., 2017; Wakamatsu et al., 2010).

Functional mutagenesis reveals the molecular basis underlying this asymmetric regulation, demonstrating a striking differential sensitivity between the DHH and DHHA1 domain interfaces. The DHHA1 interface plays a predominant role in maintaining asymmetric catalytic regulation, as its disruption through targeted mutations (D535R/F536A and Y539A/R540D) severely compromises enzymatic activity. In stark contrast, the DHH interface exhibits remarkable tolerance to structural perturbations, with mutations (T508A/S509A/R510D and T511A/F512A/D513R) showing minimal effects on

catalytic function. This differential sensitivity provides strong experimental validation for our model of inter-protomer coupling, where the structural stability of one DHHA1 domain directly influences the catalytic competence of its partner through the critical dimerization interface. We propose that the closure of one DHH-DHHA1 monomer likely pulls the partnered DHHA1 domain via this interface, compelling the second monomer to adopt a more open conformation. Such asymmetric dynamics drive a coordinated mechanism we term “asymmetric catalytic coupling,” where substrate binding and closure for catalysis at one DHH-DHHA1 pocket coincide with product release at the other through its opening. This finely tuned regulatory architecture maintains a critical balance, preventing excessive c-di-AMP depletion while ensuring sufficient enzymatic turnover, which is vital for bacterial survival under stress conditions requiring precise control of c-di-AMP levels.

Non-canonical GGDEF domain functions as a novel tetrameric scaffolding hub

SmGdpP$_{74}$’s non-canonical GGDEF domain, bearing an NMDRF motif instead of the canonical GGDEF sequence, functions primarily as a structural scaffold via tetrameric assembly rather than as a diguanylate cyclase as in the case of WspR (De et al., 2009) or DgcR (Teixeira et al., 2021). Tetramerization, mediated by the diagonal α3-helix stacking, is indispensable for catalytic activity, as R219D/R220D mutations at the diagonal GGDEF–GGDEF interface ablate phosphodiesterase function. This scaffold facilitates substrate-activated conformational selection by positioning GGDEF domains to engage the DHH-DHHA1 core: conserved residues D293 and N183 in GGDEF form hydrogen bonds with DHH residues, stabilizing the closed, active protomer. Additionally, GGDEF residues L288 and N285 interact with the linker’s R319-S320-R321 segment, effectively bridging the tetramer and maintaining active-site geometry during catalysis. This represents the first detailed example of a GGDEF domain repurposed as a heterologous scaffold, expanding the functional repertoire of degenerate GGDEF domains beyond c-di-GMP synthesis. Evolutionary parallels arise in Hypr GGDEFs, where cross-dimer contacts enable cGAMP synthesis, highlighting convergent use of oligomeric interfaces for regulation. Furthermore, GGDEF domains in *Staphylococcus aureus* recruit diacylglycerol kinase to the membrane, suggesting that such scaffolds may broadly serve as interaction hubs in bacterial signaling (Mychack et al., 2025).

SmGdpP$_{74}$ heme-CN conformation likely to represent heme inhibited state

The PAS domain functions as a dynamic sensor of signaling molecules, using heme coordination to modulate DHH-DHHA1 activity. In the apo state, PAS mobility occludes high-resolution structural capture, consistent with its role as a dynamic sensor sampling multiple conformational states (Gilles-Gonzalez and Gonzalez, 2004). The differential

effects of heme versus heme-CN on $SmGdpP_{74}$ activity (Figure 1E) can be explained through two potential mechanisms: heme-CN binding might induce a partially active state via interdomain conformational changes, or alternatively, the PAS domain may bind heme-CN with lower affinity than heme, resulting in reduced inhibition. However, the first scenario appears unlikely, as there is no evidence of significant conformational changes induced by heme-CN compared to heme alone. For example, in the heme-responsive protein PefR of the MarR family, heme binding causes substantial conformational shifts in the DNA-binding domains, yet the heme-CN-bound structure remains nearly identical to the heme-bound form (Nishinaga et al., 2021). Similarly, in truncated Mtb N-terminal hemoglobin and *Drosophila melanogaster* hexacoordinate hemoglobin, conformational changes with CN^- are limited to the heme-binding active site residues compared to their heme-bound counterparts (de Sanctis et al., 2006; Milani et al., 2004). Therefore, it is more plausible that the reversal of heme inhibition by heme-CN results from its lower affinity for the heme-binding pocket. Furthermore, the physiological relevance of CN^- in most bacteria is questionable due to its toxicity, as it inhibits cytochrome c oxidase and disrupts aerobic respiration. It also suppresses the growth of *S. aureus* and other cyanide-sensitive bacteria (Létoffé et al., 2022). Given this physiological context, it is improbable that bacterial proteins would adopt a distinct conformational state for heme-CN compared to heme. The notable conformational changes observed in the heme-CN state of $SmGdpP_{74}$ are therefore likely to mirror those induced by heme alone, suggesting that our heme-CN structure most probably mimics the inhibited state of SmGdpP in the presence of heme. In conclusion, these findings highlight the need for further studies to confirm the binding affinities of heme and heme-CN to $SmGdpP_{74}$ and to explore whether these conformational similarities hold under physiological conditions, providing deeper insights into the regulatory mechanisms of phosphodiesterase activity in bacterial systems.

Potential heme-binding site at the DHH-DHHA1 interface

We observed an unidentified electron density within the DHH-DHHA1 catalytic pocket that closely resembles heme; however, due to resolution limitations, we could not conclusively assign it as such (Figure S5). Initial modeling positioned the iron atom of the putative heme directly above a conserved histidine residue (H623), suggesting the possibility of incidental heme binding. This histidine is the terminal residue of the GGGH motif, a sequence commonly found in DHH-DHHA1 domains and known to interact with the adenine ring of cyclic di-AMP via π-π stacking (He et al., 2016; Wang et al., 2018). Given that heme iron is often coordinated by conserved histidine residues, the observed density at the DHH-DHHA1 interface, immediately above this residue, could indicate a secondary heme-binding site, perhaps resulting from high heme concentrations (10 fold molar excess) during sample preparation.

Notably, both *Bacillus subtilis* (Bs) $GdpP_{84-659}$ and *Geobacillus thermodenitrificans* (Gt) $GdpP_{55-658}$ have been reported to bind heme with a 1:1 stoichiometry, whereas a construct containing only the PAS domain of Gt $GdpP_{55-162}$ exhibits a significantly lower heme-to-protein ratio (Rao et al., 2011). Since GdpP is a tetramer and each PAS domain dimer is expected to bind only one heme molecule, exclusive PAS-mediated heme binding would yield a heme-to-protein ratio of 0.5, not 1 (Tan et al., 2013). Therefore, the observed stoichiometry in both Bs and Gt cytosolic GdpP could be explained if each of the two DHH-DHHA1 domains may also accommodate a heme molecule at the active site. Additionally, structural modeling of full-length SmGdpP with heme revealed heme binding at the DHH-DHHA1 catalytic site (structure not shown), in a manner similar to our tentative heme model. In the AlphaFold model, the macrocycle of heme is coordinated by His623, supporting the proposed binding mode. Whether this site represents a secondary, lower-affinity heme-binding location compared to the PAS domain requires careful evaluation as the current resolution precludes definitive assignment of this density in the atomic model. Future work should include higher-resolution structural studies and targeted biochemical assays to confirm heme binding at this site, characterize its affinity and specificity, and clarify its potential role in regulating DHH-DHHA1 domain function under physiological conditions.

Mechanistic model for $SmGdpP_{74}$ regulation

Based on the structural and functional data we have gathered, we propose a detailed model for the catalytic cycle and regulation of $SmGdpP_{74}$. The apo conformation represents a transient, open state where the DHH-DHHA1 catalytic pockets are accessible for both substrate binding and product release. Given the asymmetric catalytic coupling and unique topology of the GGDEF scaffolding, the most efficient mechanism for $SmGdpP_{74}$ to hydrolyze c-di-AMP involves binding two c-di-AMP molecules at diagonally opposite DHH-DHHA1 active sites, as depicted in Figure 11. In the initial phase (step 1 of Figure 11), c-di-AMP binds to the GGGH motif of the two diagonal DHHA1 domains in the apo conformation, initiating closure of the DHH-DHHA1 pockets. This closure is coordinated with the tetramerization of the GGDEF domains, which scaffold the DHH-DHHA1 domains to catalyze the conversion of c-di-AMP into 5’-pApA. This results in an active conformation, similar to our observed 5’-pApA-bound structure, where one DHH-DHHA1 pocket is fully closed while the other remains open (step 2). This active state is likely energetically favored due to the protein adopting a more compact configuration with reduced solvent-exposed surface area and increased interdomain interactions compared to the apo state. Additionally, the 5’-pApA in the active site pocket may act as a stabilizing nano-RNA-like cofactor, enhancing the stability of the protein within the pocket (Fang et al., 2009). For the catalytic cycle to continue, 5’-pApA must be

released from the active site through the reopening of the DHH-DHHA1 pocket. We propose that the binding of another pair of c-di-AMP molecules to the DHHA1 domains of the neighboring open conformation (step 2) triggers a transition back to the apo state (step 3), effectively pulling the protein out of its energetically favored active state. This conformational change acts as a reset step. It would not only enable the release of the stably bound 5'-pApA from the active pocket through asymmetric coupling, but also allows the GGDEF domains to re-tetramerize in the opposite fashion, scaffolding the previously unoccupied DHH-DHHA1 pockets now bound to c-di-AMP for hydrolysis (step 4). Subsequently, two new c-di-AMP molecules bind to the open DHHA1 domains, prompting the protein to return to the apo state (step 1), perpetuating the cycle until c-di-AMP is depleted.

Our model also offers a clear and direct explanation for KRSR motif-mediated inhibition by heme. Heme-CN (or heme) binding stabilizes the typically flexible PAS domain, as evidenced by significant unresolved density, likely corresponding to the PAS domain, near the two diagonal DHH-DHHA1 domains (Figure 4A). Given that GdpP PAS domains form dimers, each PAS dimer interacts with only one DHH-DHHA1 domain on each side, leaving the other pair unengaged. This raises the question of how heme-bound PAS can inhibit the enzyme while directly contacting only half of the catalytic domains. We propose (Figure 11) that heme binding enables the PAS domain to engage the diagonally positioned DHH domains through the KRSR motif. This interaction conformationally traps these domains, preventing the necessary transition back to the apo conformation required for product release or further substrate hydrolysis. As a result, the enzyme remains inhibited, illustrating how selective stabilization and domain locking by the PAS-KRSR interaction effectively halts the catalytic cycle.

This dynamic model of substrate binding, conformational transitions, and product release depends on a highly flexible linker region. Our data demonstrate that even a subtle mutation, substituting the double glycine motif with alanines in the linker, significantly impairs enzymatic activity (Figure 9B). This finding supports the idea that $SmGdpP_{74}$ requires substantial domain rotation during its catalytic cycle. According to our model, product release from the active site is triggered when a substrate binds at the neighboring site, a process facilitated by the asymmetric coupling mechanism governed by the DHHA1 interface. Following each round of diagonal hydrolysis, the enzyme resets to its apo conformation, enabling the GGDEF domain to change its conformation to scaffold the previously inactive, now c-di-AMP–bound, DHH-DHHA1 domain for efficient hydrolysis. While this model logically integrates the conformational changes we observed with our functional data, it remains subject to revision as more comprehensive structural and biochemical data become available for each step of the hydrolysis cycle.

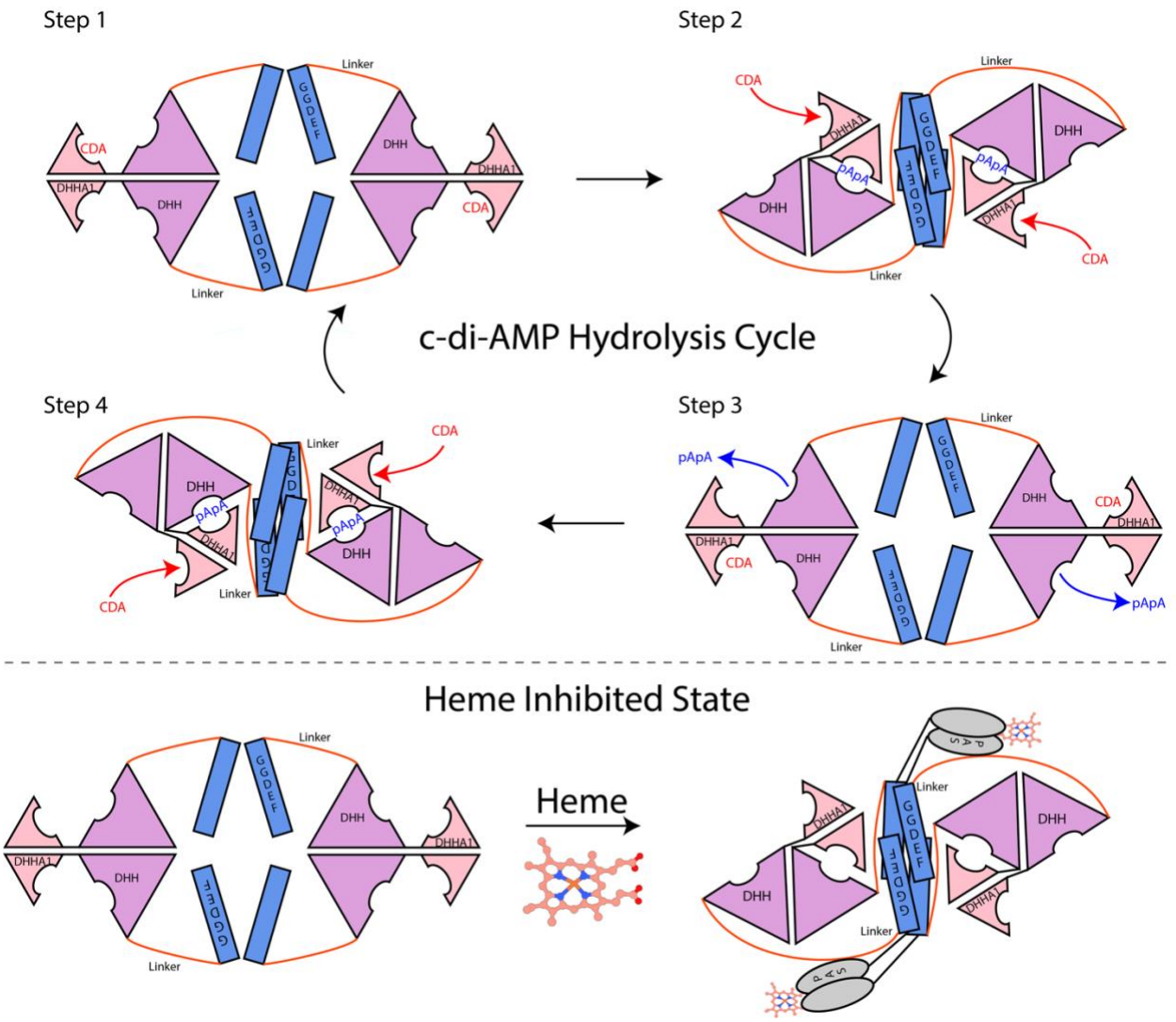

Figure 11: Cartoon illustration of the proposed mechanistic model for the c-di-AMP hydrolysis cycle and heme inhibition. Domains are colored and labelled as previous figures. C-di-AMP is denoted as CDA (red) and 5'-pAPA is denoted as pApA (blue). For clarity, domains from only one protomer chain is labelled on each site. Heme-inhibited state (below dashed line) highlights holo-PAS domain binding to the DHH domain via the linker. PAS domains are not shown except for the heme-bound state due to the lack of structural evidence for the PAS in the apo (Figure 2A) and 5'-pApA conformations (Figure 5A).

The GGDEF-DHH linker: A sophisticated allosteric control element

The GGDEF-DHH linker region of $SmGdpP_{74}$ represents a paradigmatic example of how short peptide segments can evolve into sophisticated regulatory switches that integrate multiple signaling pathways. Our structural and functional analyses reveal that this 12-residue segment (G310-R321) functions as both a flexible mechanical coupling element

and a conformationally sensitive molecular switch, orchestrating the complex interplay between environmental sensing, domain dynamics, and asymmetric catalytic regulation.

The linker's dual functionality stems from its strategically positioned glycine residues and conserved sequence motifs. The N-terminal glycines (G310 and G311) provide the backbone flexibility essential for facilitating the large-scale conformational transitions observed between distinct enzymatic states. Our mutagenesis studies demonstrate a direct correlation between linker rigidity and functional impairment: progressive substitutions to bulkier residues dramatically compromise function, with GG310VV mutations causing 93% activity loss. This exceptional sensitivity underscores the precision required for the conformational transitions that enable asymmetric catalytic coupling. The conserved KRSR motif within the linker functions as a critical molecular switch that specifically mediates heme-dependent allosteric inhibition without affecting basal catalytic activity. The complete abolition of heme-mediated inhibition in this mutant demonstrates the motif's specific role in stabilizing PAS-DHH interactions required for allosteric regulation.

Clinical implications and therapeutic potential

The essential role of GdpP in bacterial stress responses and antibiotic resistance makes it an attractive therapeutic target for combating multidrug-resistant infections. Loss-of-function GdpP mutations in clinical isolates lead to elevated c-di-AMP levels, increased β-lactam tolerance through enhanced cell wall synthesis, and enhanced biofilm formation that complicates treatment outcomes. The detailed structural insights from $SmGdpP_{74}$ provide a foundation for rational drug design targeting the allosteric regulatory mechanisms rather than the catalytic site alone, potentially offering new approaches to restore antibiotic sensitivity.

The tetrameric architecture and heme regulation unique to GdpP distinguish it from other c-di-AMP phosphodiesterases, offering opportunities for selective inhibition without affecting host cell metabolism. Novel therapeutic strategies include targeting the differential sensitivity of DHH versus DHHA1 dimerization interfaces for selective bacterial targeting, where compounds could exploit the critical role of the DHHA1 interface in maintaining asymmetric regulation. Given that similar DHHA1-mediated coupling mechanisms likely exist in standalone DHH-DHHA1 proteins across diverse bacterial species, therapeutic approaches targeting DHHA1 interfaces could have broad antimicrobial applications (Wang et al., 2024). Additional approaches include compounds that disrupt GGDEF tetramerization interfaces or interfere with PAS domain signaling through the conserved linker. The linker represents a particularly attractive target, as

compounds disrupting PAS-DHH interactions could prevent allosteric inhibition while preserving basal catalytic activity. This approach represents a paradigm shift toward targeting protein conformational dynamics rather than traditional active site inhibition, potentially overcoming resistance mechanisms that affect conventional antibiotics.

CRedit author statement

Shadikejiang Shataer: Conceptualization, Methodology, Investigation, Validation, Formal analysis, Data curation, Visualization, Writing – original draft, Writing – review & editing. **Shannon Modla**: Investigation. **Leif Boddie**: Investigation, Writing – review & editing. **Samiran Subedi**: Investigation. **Katsuhiko Murakami**: Investigation, Formal analysis. **Mona Batish**: Funding acquisition, Project administration. **Vijay Parashar**: Conceptualization, Formal analysis, Writing – review & editing, Supervision, Project administration, Funding acquisition.

Declaration of competing interest

The authors declare that they have no known competing financial interests or personal relationships that could have appeared to influence the work reported in this paper.

Acknowledgements and Funding Information

This research was funded by National Institute of Health, grant number R35GM119504 to V.P. and National Science Foundation, grant number 2244127 funds to M.B. and V.P. We thank the bioimaging center of Delaware Biotechnology Institute for providing sample screening access. Microscopy access was supported by grants from the NIH-NIGMS (P20 GM103446), the NIGMS (P20 GM139760) and the State of Delaware. This project was supported by the Delaware INBRE program, with a grant from the National Institute of General Medical Sciences – NIGMS (P20 GM103446) from the National Institutes of Health and the State of Delaware. We thank Jake Kaminsky, Guobin Hu, Liguo Wang from the laboratory of biomolecular structure at the Brookhaven national laboratory for their help with Cryo-EM data collection. The Laboratory for BioMolecular Structure (LBMS) is supported by the DOE Office of Biological and Environmental Research (KP1607011). Some of Cryo-EM screening was performed at the National Center for CryoEM Access and Training (NCCAT) and the Simons Electron Microscopy Center located at the New York Structural Biology Center, supported by the NIH Common Fund Transformative High Resolution Cryo-Electron Microscopy program (U24 GM129539,

and NIGMS R24 GM154192) and by grants from the Simons Foundation (SF349247) and NY State Assembly. We thank Dr. Richard Knappenberger for his help with analytical ultra-centrifugation.

References

Bai, Y., Yang, J., Eisele, L.E., Underwood, A.J., Koestler, B.J., Waters, C.M., Metzger, D.W., Bai, G., 2013. Two DHH subfamily 1 proteins in Streptococcus pneumoniae possess cyclic di-AMP phosphodiesterase activity and affect bacterial growth and virulence. J. Bacteriol. 195, 5123–5132. https://doi.org/10.1128/JB.00769-13

Bailey, T.L., Johnson, J., Grant, C.E., Noble, W.S., 2015. The MEME Suite. Nucleic Acids Res. 43, W39–W49. https://doi.org/10.1093/nar/gkv416

Bowman, L., Zeden, M.S., Schuster, C.F., Kaever, V., Gründling, A., 2016. New Insights into the Cyclic Di-adenosine Monophosphate (c-di-AMP) Degradation Pathway and the Requirement of the Cyclic Dinucleotide for Acid Stress Resistance in Staphylococcus aureus. J. Biol. Chem. 291, 26970–26986. https://doi.org/10.1074/jbc.M116.747709

Brautigam, C.A., 2015. Calculations and Publication-Quality Illustrations for Analytical Ultracentrifugation Data. Methods Enzymol. 562, 109–133. https://doi.org/10.1016/bs.mie.2015.05.001

Chan, C., Paul, R., Samoray, D., Amiot, N.C., Giese, B., Jenal, U., Schirmer, T., 2004. Structural basis of activity and allosteric control of diguanylate cyclase. Proc. Natl. Acad. Sci. 101, 17084–17089. https://doi.org/10.1073/pnas.0406134101

Cho, K.H., Kang, S.O., 2013. Streptococcus pyogenes c-di-AMP Phosphodiesterase, GdpP, Influences SpeB Processing and Virulence. PLOS ONE 8, e69425. https://doi.org/10.1371/journal.pone.0069425

Commichau, F.M., Heidemann, J.L., Ficner, R., Stülke, J., 2018. Making and Breaking of an Essential Poison: the Cyclases and Phosphodiesterases That Produce and Degrade the Essential Second Messenger Cyclic di-AMP in Bacteria. J. Bacteriol. 201, 10.1128/jb.00462-18. https://doi.org/10.1128/jb.00462-18

Corrigan, R.M., Bowman, L., Willis, A.R., Kaever, V., Gründling, A., 2015. Cross-talk between two nucleotide-signaling pathways in Staphylococcus aureus. J. Biol. Chem. 290, 5826–5839. https://doi.org/10.1074/jbc.M114.598300

Corrigan, R.M., Gründling, A., 2013. Cyclic di-AMP: another second messenger enters the fray. Nat. Rev. Microbiol. 11, 513–524. https://doi.org/10.1038/nrmicro3069

De, N., Navarro, M.V.A.S., Raghavan, R.V., Sondermann, H., 2009. Determinants for the activation and autoinhibition of the diguanylate cyclase response regulator WspR. J. Mol. Biol. 393, 619–633. https://doi.org/10.1016/j.jmb.2009.08.030

de Sanctis, D., Ascenzi, P., Bocedi, A., Dewilde, S., Burmester, T., Hankeln, T., Moens, L., Bolognesi, M., 2006. Cyanide binding and heme cavity conformational transitions in Drosophila melanogaster hexacoordinate hemoglobin. Biochemistry 45, 10054–10061. https://doi.org/10.1021/bi060462a

Deepthi, A., Liew, C.W., Liang, Z.-X., Swaminathan, K., Lescar, J., 2014. Structure of a diguanylate cyclase from Thermotoga maritima: insights into activation, feedback inhibition and thermostability. PloS One 9, e110912. https://doi.org/10.1371/journal.pone.0110912

Du, B., Ji, W., An, H., Shi, Y., Huang, Q., Cheng, Y., Fu, Q., Wang, H., Yan, Y., Sun, J., 2014. Functional analysis of c-di-AMP phosphodiesterase, GdpP, in *Streptococcus suis* serotype 2. Microbiol. Res. 169, 749–758. https://doi.org/10.1016/j.micres.2014.01.002

Emsley, P., Lohkamp, B., Scott, W.G., Cowtan, K., 2010. Features and development of *Coot*. Acta Crystallogr. D Biol. Crystallogr. 66, 486–501. https://doi.org/10.1107/S0907444910007493

Fang, M., Zeisberg, W.-M., Condon, C., Ogryzko, V., Danchin, A., Mechold, U., 2009. Degradation of nanoRNA is performed by multiple redundant RNases in Bacillus subtilis. Nucleic Acids Res. 37, 5114–5125. https://doi.org/10.1093/nar/gkp527

Gilles-Gonzalez, M.-A., Gonzalez, G., 2004. Signal transduction by heme-containing PAS-domain proteins. J. Appl. Physiol. 96, 774–783. https://doi.org/10.1152/japplphysiol.00941.2003

Griffiths, J.M., O'Neill, A.J., 2012. Loss of Function of the GdpP Protein Leads to Joint β-Lactam/Glycopeptide Tolerance in Staphylococcus aureus. Antimicrob. Agents Chemother. 56, 579–581. https://doi.org/10.1128/AAC.05148-11

Gundlach, J., Mehne, F.M.P., Herzberg, C., Kampf, J., Valerius, O., Kaever, V., Stülke, J., 2015. An Essential Poison: Synthesis and Degradation of Cyclic Di-AMP in Bacillus subtilis. J. Bacteriol. 197, 3265–3274. https://doi.org/10.1128/jb.00564-15

He, J., Yin, W., Galperin, M.Y., Chou, S.-H., 2020. Cyclic di-AMP, a second messenger of primary importance: tertiary structures and binding mechanisms. Nucleic Acids Res. 48, 2807–2829. https://doi.org/10.1093/nar/gkaa112

He, Q., Wang, F., Liu, S., Zhu, D., Cong, H., Gao, F., Li, B., Wang, H., Lin, Z., Liao, J., Gu, L., 2016a. Structural and Biochemical Insight into the Mechanism of Rv2837c from Mycobacterium tuberculosis as a c-di-NMP Phosphodiesterase. J. Biol. Chem. 291, 3668–3681. https://doi.org/10.1074/jbc.M115.699801

He, Q., Wang, F., Liu, S., Zhu, D., Cong, H., Gao, F., Li, B., Wang, H., Lin, Z., Liao, J., Gu, L., 2016b. Structural and Biochemical Insight into the Mechanism of Rv2837c from Mycobacterium tuberculosis as a c-di-NMP Phosphodiesterase. J. Biol. Chem. 291, 3668–3681. https://doi.org/10.1074/jbc.M115.699801

Huynh, T.N., Luo, S., Pensinger, D., Sauer, J.-D., Tong, L., Woodward, J.J., 2015. An HD-domain phosphodiesterase mediates cooperative hydrolysis of c-di-AMP to affect bacterial growth and virulence. Proc. Natl. Acad. Sci. U. S. A. 112, E747-756. https://doi.org/10.1073/pnas.1416485112

Jumper, J., Evans, R., Pritzel, A., Green, T., Figurnov, M., Ronneberger, O., Tunyasuvunakool, K., Bates, R., Žídek, A., Potapenko, A., Bridgland, A., Meyer, C., Kohl, S.A.A., Ballard, A.J., Cowie, A., Romera-Paredes, B., Nikolov, S., Jain, R., Adler, J., Back, T., Petersen, S., Reiman, D., Clancy, E., Zielinski, M., Steinegger, M., Pacholska, M., Berghammer, T., Bodenstein, S., Silver, D., Vinyals, O., Senior, A.W., Kavukcuoglu, K., Kohli, P., Hassabis, D., 2021. Highly accurate protein structure prediction with AlphaFold. Nature 596, 583–589. https://doi.org/10.1038/s41586-021-03819-2

Latoscha, A., Drexler, D.J., Al-Bassam, M.M., Bandera, A.M., Kaever, V., Findlay, K.C., Witte, G., Tschowri, N., 2020. c-di-AMP hydrolysis by the phosphodiesterase AtaC promotes differentiation of multicellular bacteria. Proc. Natl. Acad. Sci. 117, 7392–7400. https://doi.org/10.1073/pnas.1917080117

Lemos, J.A., Palmer, S.R., Zeng, L., Wen, Z.T., Kajfasz, J.K., Freires, I.A., Abranches, J., Brady, L.J., 2019. The Biology of Streptococcus mutans. Microbiol. Spectr. 7, 10.1128/microbiolspec.gpp3-0051–2018. https://doi.org/10.1128/microbiolspec.gpp3-0051-2018

Létoffé, S., Wu, Y., Darch, S.E., Beloin, C., Whiteley, M., Touqui, L., Ghigo, J.-M., 2022. Pseudomonas aeruginosa Production of Hydrogen Cyanide Leads to Airborne Control of Staphylococcus aureus Growth in Biofilm and In Vivo Lung Environments. mBio 13, e0215422. https://doi.org/10.1128/mbio.02154-22

Liebschner, D., Afonine, P.V., Baker, M.L., Bunkóczi, G., Chen, V.B., Croll, T.I., Hintze, B., Hung, L.-W., Jain, S., McCoy, A.J., Moriarty, N.W., Oeffner, R.D., Poon, B.K., Prisant, M.G., Read, R.J., Richardson, J.S., Richardson, D.C., Sammito, M.D., Sobolev, O.V., Stockwell, D.H., Terwilliger, T.C., Urzhumtsev, A.G., Videau, L.L., Williams, C.J., Adams, P.D., 2019. Macromolecular structure determination using X-rays, neutrons and electrons: recent developments in Phenix. Acta Crystallogr. Sect. Struct. Biol. 75, 861–877. https://doi.org/10.1107/S2059798319011471

Manikandan, K., Sabareesh, V., Singh, N., Saigal, K., Mechold, U., Sinha, K.M., 2014. Two-Step Synthesis and Hydrolysis of Cyclic di-AMP in Mycobacterium tuberculosis. PLOS ONE 9, e86096. https://doi.org/10.1371/journal.pone.0086096

Milani, M., Ouellet, Y., Ouellet, H., Guertin, M., Boffi, A., Antonini, G., Bocedi, A., Mattu, M., Bolognesi, M., Ascenzi, P., 2004. Cyanide Binding to Truncated Hemoglobins: A Crystallographic and Kinetic Study,. Biochemistry 43, 5213–5221. https://doi.org/10.1021/bi049870+

Mychack, A., Evans, D., Gilles, T., James, M.J., Walker, S., 2025. Staphylococcus aureus uses a GGDEF protein to recruit diacylglycerol kinase to the membrane for lipid recycling. Proc. Natl. Acad. Sci. U. S. A. 122, e2414696122. https://doi.org/10.1073/pnas.2414696122

Nishinaga, M., Sugimoto, H., Nishitani, Y., Nagai, S., Nagatoishi, S., Muraki, N., Tosha, T., Tsumoto, K., Aono, S., Shiro, Y., Sawai, H., 2021. Heme controls the structural rearrangement of its sensor protein mediating the hemolytic bacterial survival. Commun. Biol. 4, 467. https://doi.org/10.1038/s42003-021-01987-5

Noble, A.J., Dandey, V.P., Wei, H., Brasch, J., Chase, J., Acharya, P., Tan, Y.Z., Zhang, Z., Kim, L.Y., Scapin, G., Rapp, M., Eng, E.T., Rice, W.J., Cheng, A., Negro, C.J., Shapiro, L., Kwong, P.D., Jeruzalmi, D., des Georges, A., Potter, C.S., Carragher, B., n.d. Routine single particle CryoEM sample and grid characterization by tomography. eLife 7, e34257. https://doi.org/10.7554/eLife.34257

Peng, X., Zhang, Y., Bai, G., Zhou, X., Wu, H., 2016. Cyclic di-AMP mediates biofilm formation. Mol. Microbiol. 99, 945–959. https://doi.org/10.1111/mmi.13277

Pettersen, E.F., Goddard, T.D., Huang, C.C., Couch, G.S., Greenblatt, D.M., Meng, E.C., Ferrin, T.E., 2004. UCSF Chimera--a visualization system for exploratory research and analysis. J. Comput. Chem. 25, 1605–1612. https://doi.org/10.1002/jcc.20084

Poon, R., Basuino, L., Satishkumar, N., Chatterjee, A., Mukkayyan, N., Buggeln, E., Huang, L., Nair, V., Argudín, M.A., Datta, S.K., Chambers, H.F., Chatterjee, S.S., n.d. Loss of GdpP Function in Staphylococcus aureus Leads to β-Lactam Tolerance and Enhanced Evolution of β-Lactam Resistance. Antimicrob. Agents Chemother. 66, e01431-21. https://doi.org/10.1128/AAC.01431-21

Punjani, A., Rubinstein, J.L., Fleet, D.J., Brubaker, M.A., 2017. cryoSPARC: algorithms for rapid unsupervised cryo-EM structure determination. Nat. Methods 14, 290–296. https://doi.org/10.1038/nmeth.4169

Rao, F., Ji, Q., Soehano, I., Liang, Z.-X., 2011. Unusual Heme-Binding PAS Domain from YybT Family Proteins. J. Bacteriol. 193, 1543–1551. https://doi.org/10.1128/JB.01364-10

Rao, F., See, R.Y., Zhang, D., Toh, D.C., Ji, Q., Liang, Z.-X., 2010. YybT is a signaling protein that contains a cyclic dinucleotide phosphodiesterase domain and a GGDEF domain with ATPase activity. J. Biol. Chem. 285, 473–482. https://doi.org/10.1074/jbc.M109.040238

Scheich, C., Kümmel, D., Soumailakakis, D., Heinemann, U., Büssow, K., 2007. Vectors for co-expression of an unrestricted number of proteins. Nucleic Acids Res. 35, e43. https://doi.org/10.1093/nar/gkm067

Schirmer, T., Jenal, U., 2009. Structural and mechanistic determinants of c-di-GMP signalling. Nat. Rev. Microbiol. 7, 724–735. https://doi.org/10.1038/nrmicro2203

Schmier, B.J., Nelersa, C.M., Malhotra, A., 2017. Structural Basis for the Bidirectional Activity of Bacillus nanoRNase NrnA. Sci. Rep. 7, 11085. https://doi.org/10.1038/s41598-017-09403-x

Schuck, P., 2000. Size-distribution analysis of macromolecules by sedimentation velocity ultracentrifugation and lamm equation modeling. Biophys. J. 78, 1606–1619. https://doi.org/10.1016/S0006-3495(00)76713-0

Sinha, S.C., Sprang, S.R., 2006. Structures, mechanism, regulation and evolution of class III nucleotidyl cyclases. Rev. Physiol. Biochem. Pharmacol. 157, 105–140. https://doi.org/10.1007/112_0603

Stülke, J., Krüger, L., 2020. Cyclic di-AMP Signaling in Bacteria. Annu. Rev. Microbiol. 74, 159–179. https://doi.org/10.1146/annurev-micro-020518-115943

Tan, E., Rao, F., Pasunooti, S., Pham, T.H., Soehano, I., Turner, M.S., Liew, C.W., Lescar, J., Pervushin, K., Liang, Z.-X., 2013. Solution Structure of the PAS Domain of a Thermophilic YybT Protein Homolog Reveals a Potential Ligand-binding Site. J. Biol. Chem. 288, 11949–11959. https://doi.org/10.1074/jbc.M112.437764

Teixeira, R.D., Holzschuh, F., Schirmer, T., 2021. Activation mechanism of a small prototypic Rec-GGDEF diguanylate cyclase. Nat. Commun. 12, 2162. https://doi.org/10.1038/s41467-021-22492-7

Vistica, J., Dam, J., Balbo, A., Yikilmaz, E., Mariuzza, R.A., Rouault, T.A., Schuck, P., 2004. Sedimentation equilibrium analysis of protein interactions with global implicit mass conservation constraints and systematic noise decomposition. Anal. Biochem. 326, 234–256. https://doi.org/10.1016/j.ab.2003.12.014

Vorobiev, S.M., Neely, H., Yu, B., Seetharaman, J., Xiao, R., Acton, T.B., Montelione, G.T., Hunt, J.F., 2012. Crystal structure of a catalytically active GG(D/E)EF diguanylate cyclase domain from Marinobacter aquaeolei with bound c-di-GMP product. J. Struct. Funct. Genomics 13, 177–183. https://doi.org/10.1007/s10969-012-9136-4

Wakamatsu, T., Kitamura, Y., Kotera, Y., Nakagawa, N., Kuramitsu, S., Masui, R., 2010. Structure of RecJ exonuclease defines its specificity for single-stranded DNA. J. Biol. Chem. 285, 9762–9769. https://doi.org/10.1074/jbc.M109.096487

Wang, F., He, Q., Su, K., Wei, T., Xu, S., Gu, L., 2018. Structural and biochemical characterization of the catalytic domains of GdpP reveals a unified hydrolysis mechanism for the DHH/DHHA1 phosphodiesterase. Biochem. J. 475, 191–205. https://doi.org/10.1042/BCJ20170739

Wang, X., Davlieva, M., Reyes, J., Panesso, D., Arias, C.A., Shamoo, Y., 2017. A Novel Phosphodiesterase of the GdpP Family Modulates Cyclic di-AMP Levels in Response to Cell Membrane Stress in Daptomycin-Resistant Enterococci. Antimicrob. Agents Chemother. 61, e01422-16. https://doi.org/10.1128/AAC.01422-16

Wang, Y., Hao, W., Guo, Z., Sun, Yiyang, Wu, Y., Sun, Yukang, Gao, T., Luo, Y., Jin, L., Yang, J., Cheng, K., 2024. Structural and functional investigation of the DHH/DHHA1 family proteins in Deinococcus radiodurans. Nucleic Acids Res. 52, 7142–7157. https://doi.org/10.1093/nar/gkae451

Zhou, J., Sayre, D.A., Zheng, Y., Szmacinski, H., Sintim, H.O., 2014. Unexpected Complex Formation between Coralyne and Cyclic Diadenosine Monophosphate Providing a Simple Fluorescent Turn-on Assay to Detect This Bacterial Second Messenger. Anal. Chem. 86, 2412–2420. https://doi.org/10.1021/ac403203x

Supplementary Information

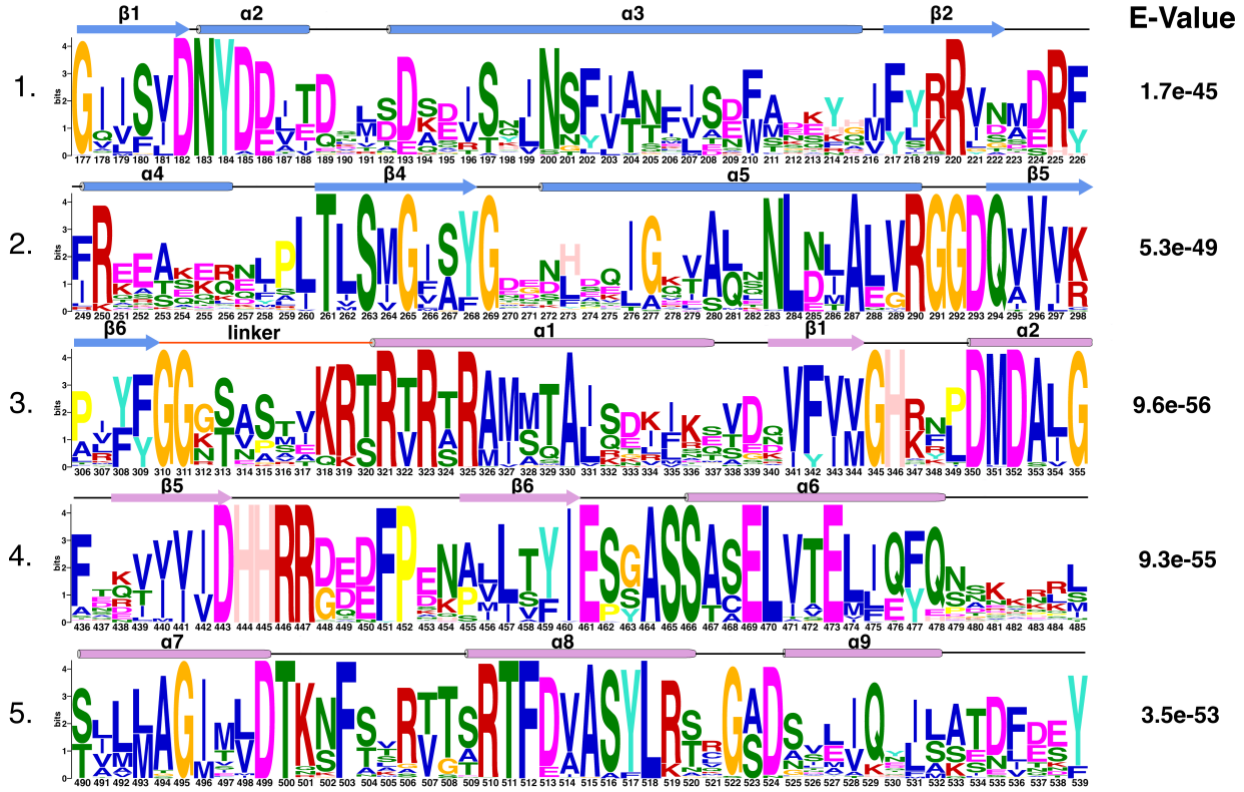

Figure S1. Sequence conservation and secondary structure mapping of GGDEF-DHH-DHHA1 domain motifs in SmGdpP$_{74}$. Sequence logos for five highly conserved motifs are shown, with residue positions indicated below each logo and secondary structure elements (α-helices and β-strands) annotated above. Motif 1 (DNYDD, panel 1) and motif 2 (RGGDQA, panel 2) highlight conserved catalytic residues within the GGDEF domain, while motif 3 (panel 3) spans the GGDEF-DHH linker and features the conserved KRSR and TRTR segments. Motifs 4 and 5 (panels 4 and 5) correspond to conserved regions in the DHH and DHHA1 domains, respectively, including the conserved DHH motif involved in catalysis. E-values to the right indicate the statistical significance of each motif's conservation.

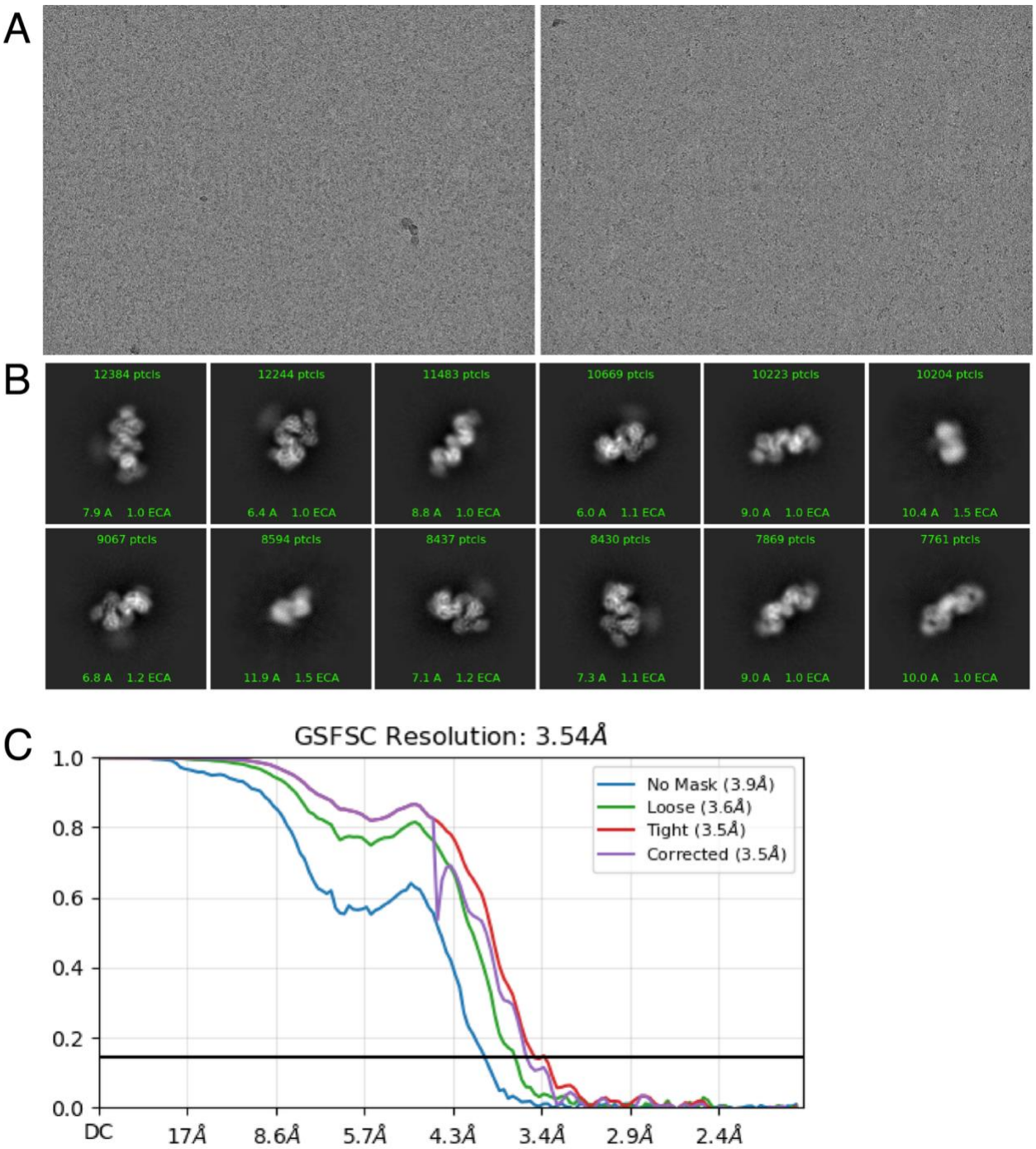

Figure S2. Cryo-EM analysis of $SmGdpP_{74}$ in the apo state. (*A*) Representative cryo-EM micrographs showing the distribution and quality of $SmGdpP_{74}$ particles in vitreous ice. (*B*) Two-dimensional class averages of particle images, with the number of particles (ptcls) and estimated resolution (Å) and effective classes assigned (ECA) indicated for each class, demonstrating a variety of particle orientations and conformational states. (*C*) Gold-standard Fourier shell correlation (GSFSC) curves for the final 3D reconstruction, showing resolution estimates with different masking strategies; the corrected GSFSC indicates a final overall resolution of 3.54 Å.

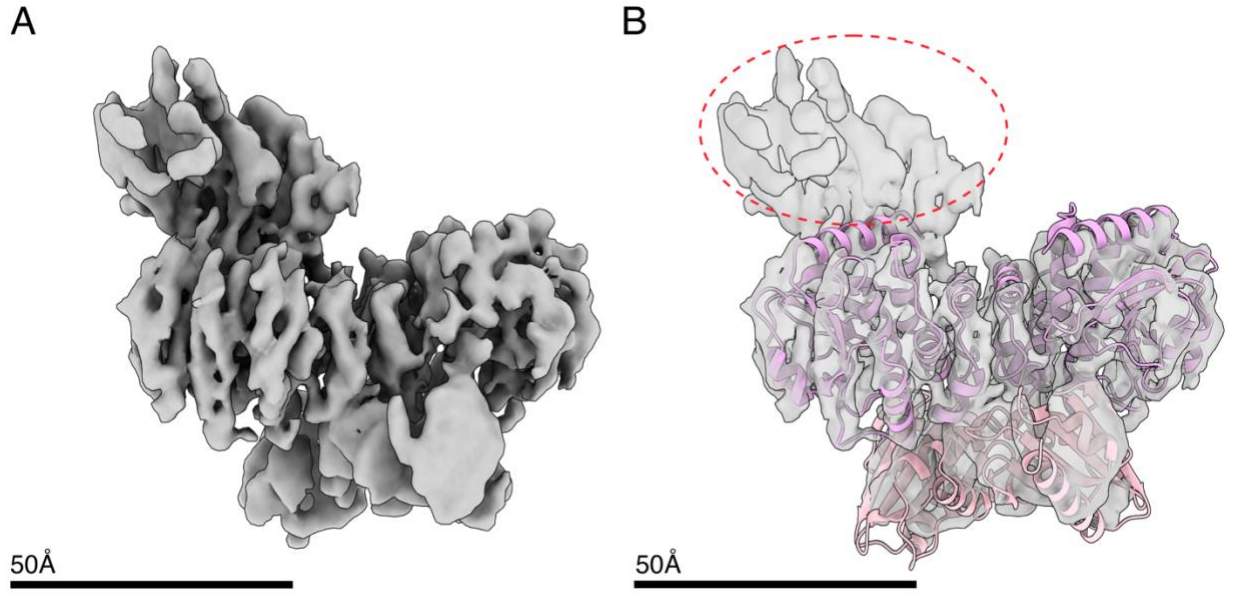

Figure S3. Low-resolution 3D density map of SmGdpP$_{74}$ fragment from multi-class cryo-EM reconstruction. (*A*) The 3D density map of the fragment displaying highly anisotropic density with low resolution. (*B*) The atomic model of the DHH-DHHA1 dimer is fitted into the density, with the DHH domain colored in purple and the DHHA1 domain in pink; unresolved regions are highlighted by red dashed circles and likely correspond to flexible or disordered areas not resolved at this resolution. Scale bars: 50 Å.

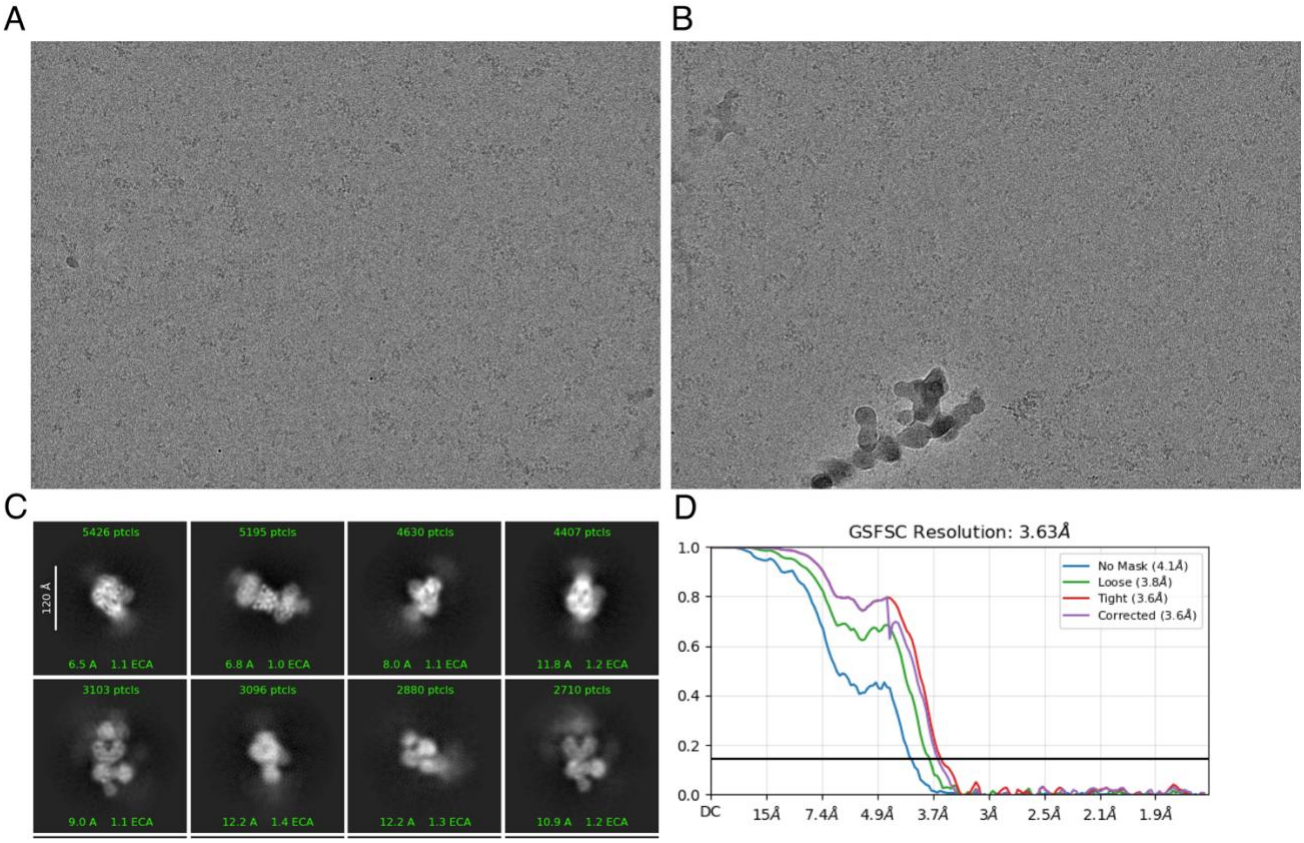

Figure S4. Cryo-EM micrographs, 2D class averages, and FSC curves for the SmGdpP$_{74}$ heme-CN dataset. (*A*-*B*) Representative Cryo-EM micrographs showing the distribution and quality of SmGdpP$_{74}$ heme-CN particles in vitreous ice. (*C*) 2D class averages from single-particle analysis displaying eight representative classes with particle numbers , along with estimated resolution (Å) and ECA values for each class, illustrating the structural homogeneity and various orientations captured in the dataset. (*D*) GSFSC curves for the final 3D reconstruction showing resolution estimates with different masking strategies, with the final overall resolution determined to be 3.63Å at the 0.143 FSC threshold.

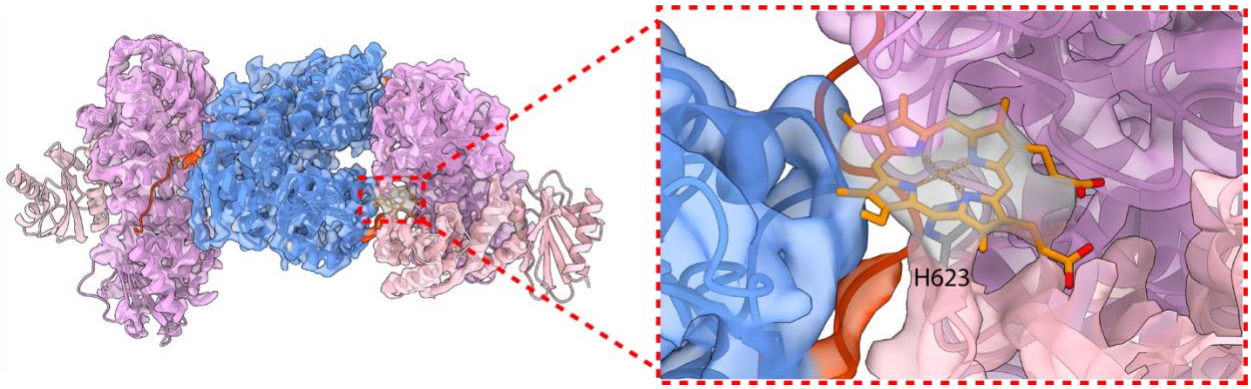

Figure S5. Cryo-EM structure of SmGdpP$_{74}$ in the presence of heme-CN with unknown density at the DHH-DHHA1 catalytic pocket. The left panel shows the atomic model (GGDEF domain: blue; linker: orange; DHH: purple; DHHA1: pink) overlaid with the Cryo-EM density map, with the conserved His623 residue labeled. The right panel highlights the catalytic pocket (dashed red box), showing the unresolved density (gray) and the tentatively fitted heme model (brown).

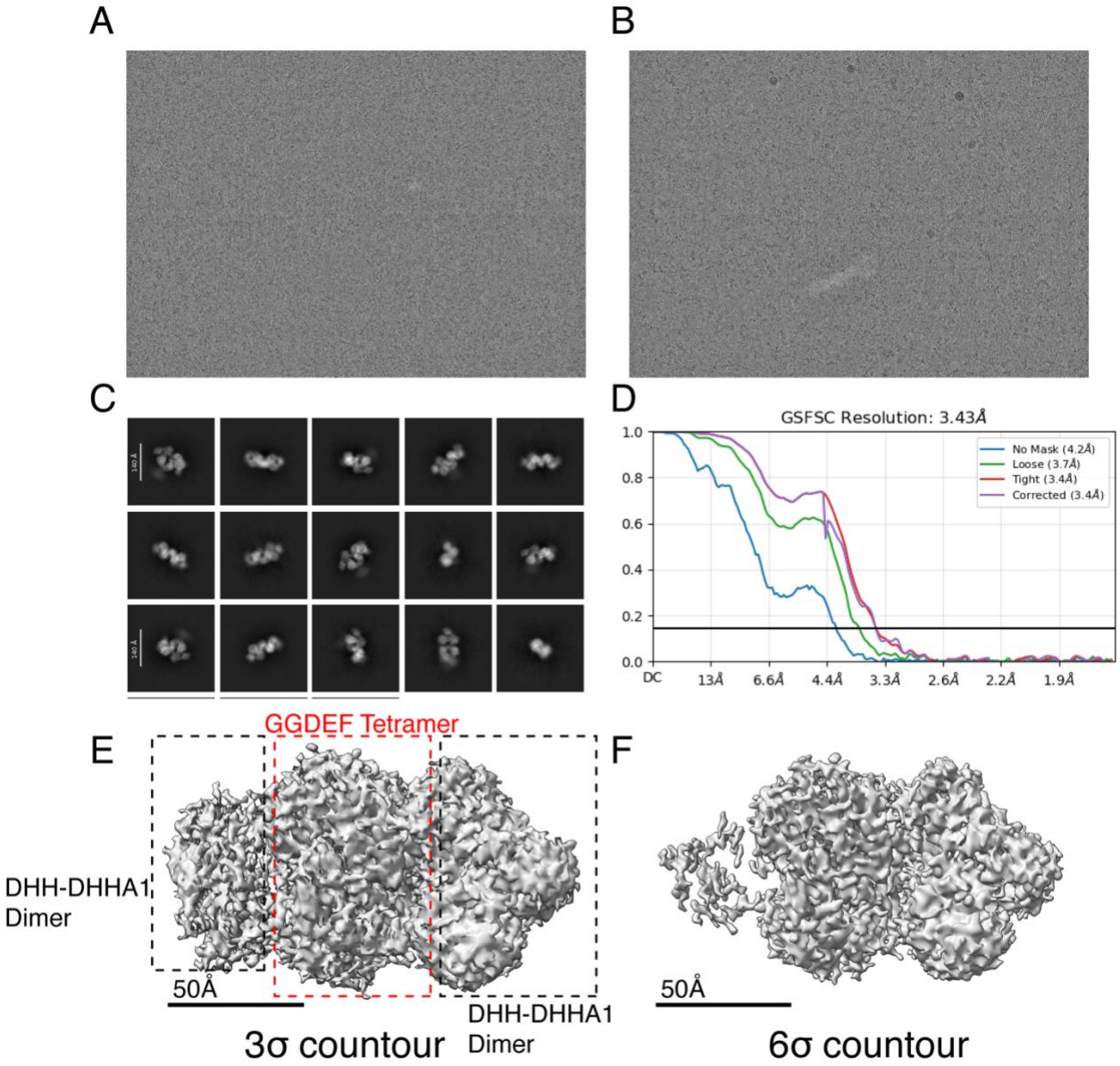

Figure S6. Cryo-EM analysis of SmGdpP$_{74}$ in complex with 5'-pApA. (*A-B*) Representative cryo-EM micrographs showing well-dispersed SmGdpP74-5'-pApA particles in vitreous ice. (*C*) Selected 2D class averages from single-particle analysis displaying fifteen representative classes with clear secondary structure features and various particle orientations. (*D*) GSFSC curves for the final 3D reconstruction showing resolution estimates with different masking strategies, yielding a final overall resolution of 3.43Å at the 0.143 FSC threshold. (*E*) 3D cryo-EM density map displayed at 3σ contour level, revealing the asymmetric architecture of the GGDEF tetramer (middle region, highlighted by red dashed box) and the catalytic DHH-DHHA1 dimer (highlighted by black dashed box). (*F*) The same reconstruction displayed at 6σ contour level, emphasizing the high-resolution core regions and the asymmetric DHH dimer on the left. Scale bars represent 50 Å in panels E and F.

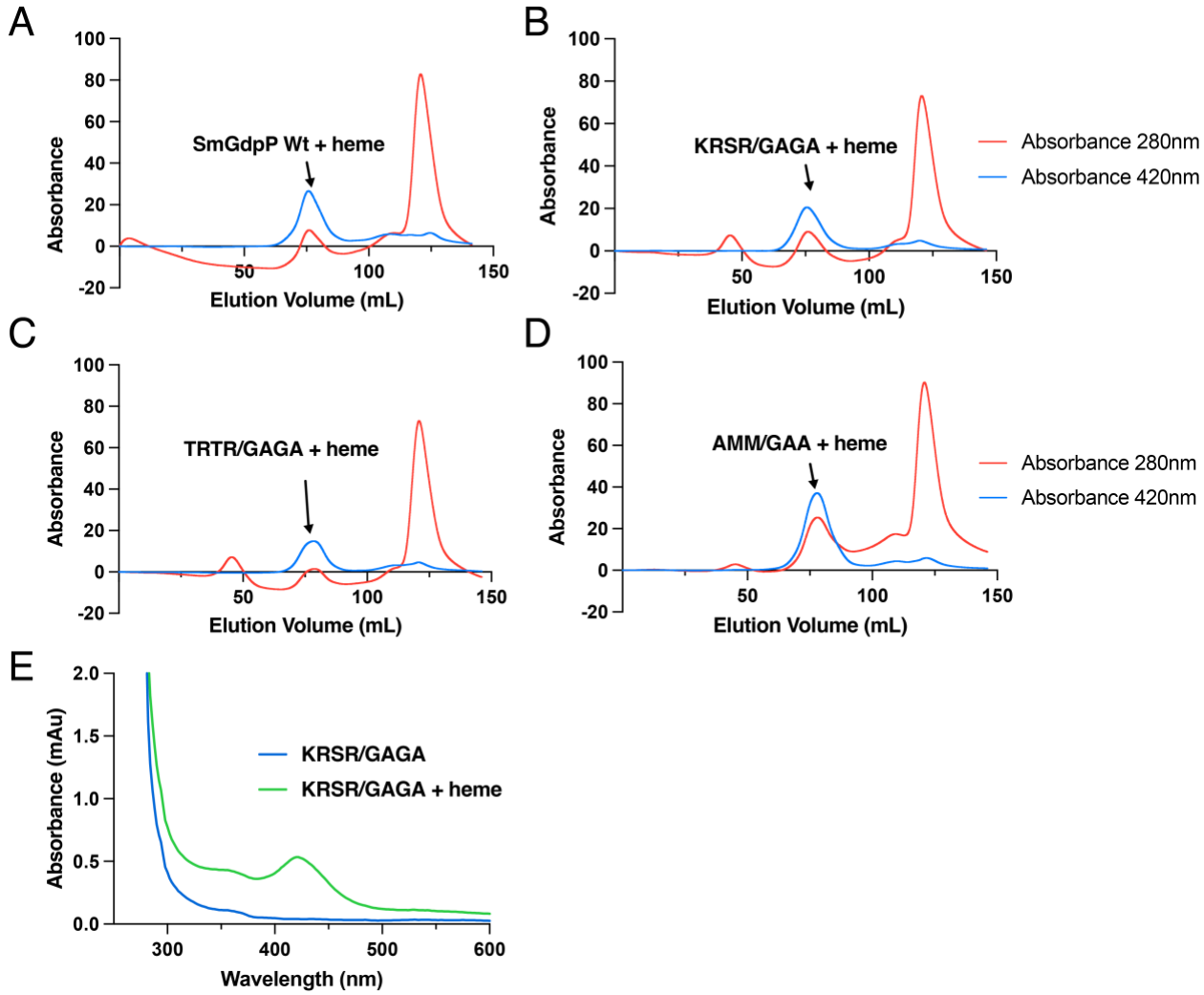

Figure S7. Size exclusion chromatography and absorbance spectroscopy analysis of heme reconstitution in SmGdpP$_{74}$ wild-type and linker mutants. (*A*-*B*) SEC profiles of heme-reconstituted wild-type and KRSR/GAGA mutant proteins are shown, with absorbance monitored at 280 nm (protein, red) and 420 nm (heme Soret band, blue); arrows indicate the elution peak corresponding to the protein-heme complex. (*C*-*D*) SEC profiles of the TRTR/GAGA and AMM/GAA mutants are similarly monitored at both wavelengths. (*E*) Absorbance spectra for the KRSR/GAGA mutant display the apo form (blue) and the heme-reconstituted form (green), highlighting spectral changes associated with heme incorporation.

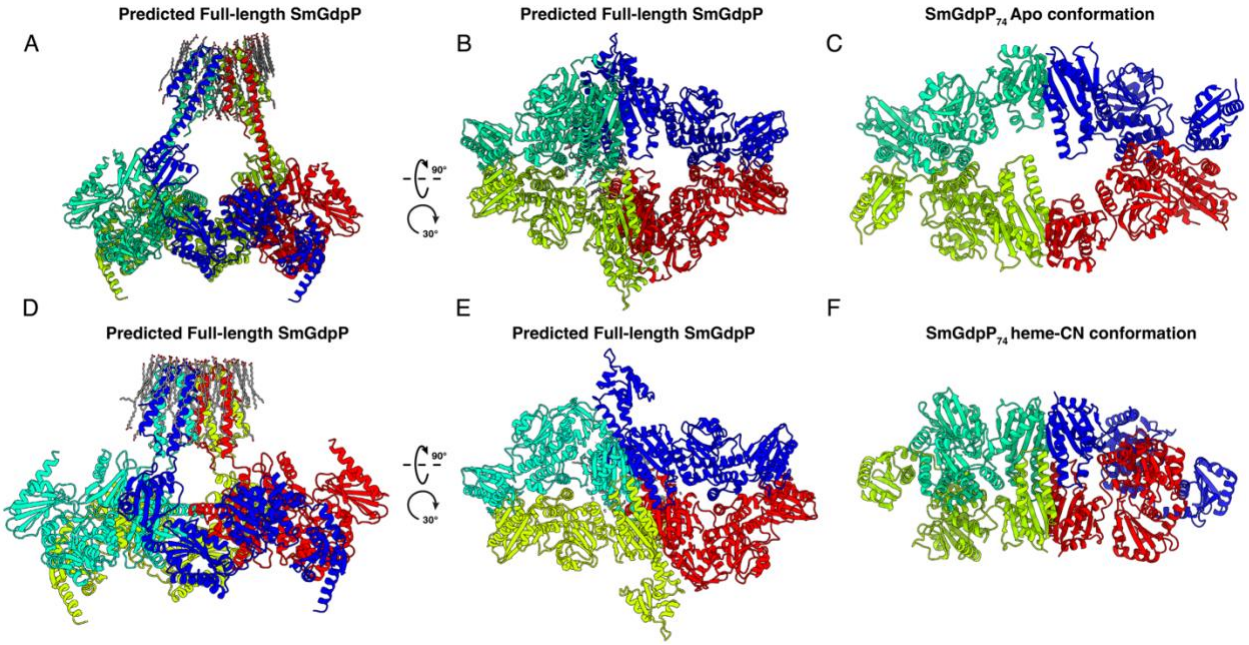

Figure S8: AlphaFold-predicted structures of full-length SmGdpP with oleic acid as a membrane mimic compared to apo and heme-CN conformations of SmGdpP$_{74}$. (*A, B*) Predicted full-length SmGdpP structures resembling the apo conformation of SmGdpP$_{74}$, with the GGDEF, DHH, and DHHA1 domains showing high structural similarity to apo SmGdpP74, though the transmembrane region adopts an extended configuration relative to the PAS domain. (*C*) Cryo-EM structure of SmGdpP$_{74}$ in the apo conformation for direct comparison. (*D, E*) Predicted full-length SmGdpP structures mirroring the heme-CN and pApA-bound conformations of SmGdpP$_{74}$, where the transmembrane region displays a more compact arrangement relative to the PAS domain. (*F*) Cryo-EM structure of SmGdpP$_{74}$ in the heme-CN conformation for reference. All structures are colored by protomer chain in red, blue, green, and yellow, respectively.

Primers	Sequences (5' to 3')
SmGdpP-PQH-FP	CACCATGGTGCTGCAGGCGGTAAGCTGATTACTATGCTTG
SmGdpP-PQH-RP	GCTCAGCTAATTAAGCTTTTAAGCTTCCTCGTTTCCTG
DN182RR-FP	CGCCGCTATGATGATACGATTGAGTC
DN182RR-RP	AATAGATATAATACCAATGACAGGTTG
RR219DD-FP	GATGATGTTAATATGGATCGTTTTTATTTC
RR219DD-RP	ATAAAAAATTTCCCTACTTTGAG
D293R-FP	CGCCAAGCTGTTATCCGTGAAAATG
D293R-RP	GCCACCACGGACAAG
TSR508AAD-FP	CCGATACCTTTGATGTAGCCAGCTAT
TSR508AAD-RP	CCGCTACACGAGTCGAGAAACTT
TFD511AAR-FP	CCCGCGTAGCCAGCTATTTACGTACG
TFD511AAR-RP	CGGCTCGGCTTGTTACACGAGT
DF535RA-FP	CGCGCGGATGAATACCGTTTAATTAAT
DF535RA-RP	AAGAGCTGAAATATTTTGAATTTCAAC
DE537RR-FP	CGCCGCTACCGTTTAATTAATGAAC
DE537RR-RP	AAAATCAAGAGCTGAAATATTTTG
YR539AD-FP	GCGGATTTAATTAATGAACTTATTTTACGT
YR539AD-RP	TTCATCAAAATCAAGAGCTGAAATAT
SK573DD-FP	GATGATGCTGCTGATACTATGTTA
SK573DD-RP	AGCAATAACATTGGAATAACTG
D384A-FP	GCGGTAGCAAGAGCTGTCAATCG
D384A-RP	ATGACTCATACTATCTTCATCATAG
H445A-FP	GCGAGAAGAGATGATGATTTTCCAG
H445A-RP	GTGATCAATCACAATAACTTC
L498A-FP	GCGGATACAAAAAGTTTCTCGACTC
L498A-RP	CATAATCCCAGCCATAACAATAC
K501A-FP	GCGAGTTTCTCGACTCGTGTAAC
K501A-RP	TGTATCAAGCATAATCCCAGC
N569A-FP	GCGGTTATTGCTAGCAAGGCTG
N569A-RP	GGAATAACTGATATCATCTGC
V570A-FP	GCGATTGCTAGCAAGGCTGCTG
V570A-RP	ATTGGAATAACTGATATCATC
S573A-FP	GCGAAGGCTGCTGATACTATGTT
S573A-RP	AGCAATAACATTGGAATAACT
KRSR/GAGA-FP	GGTGCGACTAGGACACGCGCTATG
KRSR/GAGA-RP	CGCACCAATAGTTGAAACTGTTCCTCCAC
TRTR/GAGA-FP	GCGGCCGCTATGATGACTGCTATTTC
TRTR/GAGA-RP	GGCCGCACGTGAACGCTTAATAGTTG
AMM/GAA-FP	GGCGACTGCTATTTCTGATAAAATTAAAACAG
AMM/GAA-RP	GCACCGCGTGTCCTAGTACGTGA
GG310AA_FP	GCGGGAACAGTTTCAACTATTAAGCG
GG310AA_RP	CGCAAAATAAAGCAGTTTCTTATGTTCGTC
GG310VV_FP	GTGGGAACAGTTTCAACTATTAAGCGTT
GG310VV_RP	CACAAAATAAAGCAGTTTCTTATGTTCGTCATT
GG310LL_FP	CTGGGAACAGTTTCAACTATTAAGCGTTC

GG310LL_RP	CAGAAAATAAAGCAGTTTCTTATGTTCGTC
G310PP_FP	CCGGGAACAGTTTCAACTATTAAGCGT
G310PP_RP	CGGAAAATAAAGCAGTTTCTTATGTTCGTC

Table S1: List of primers used for the construction of the wild-type (SmGdpP-PQH) and mutant plasmids.